

Infrared power-law galaxies in the Chandra Deep Field South: AGN and ULIRGs

A. Alonso-Herrero^{1,2}, P. G. Pérez-González², D. M. Alexander³, G. H. Rieke², D. Rigopoulou⁴, E. Le Floch², P. Barmby⁵, C. Papovich², J. R. Rigby², F. E. Bauer⁶, W. N. Brandt⁷, E. Egami², S. P. Willner⁵, H. Dole^{8,2}, J.-S. Huang⁵

ABSTRACT

We investigate the nature of a sample of 92 *Spitzer*/MIPS $24\mu\text{m}$ selected galaxies in the CDFS, showing power law-like emission in the *Spitzer*/IRAC 3.6– $8\mu\text{m}$ bands. The main goal is to determine whether the galaxies not detected in X-rays (47% of the sample) are part of the hypothetical population of obscured AGN not detected even in deep X-ray surveys. The majority of the IR power-law galaxies are ULIRGs at $z > 1$, and those with LIRG-like IR luminosities are usually detected in X-rays. The optical to IR spectral energy distributions (SEDs) of the X-ray detected galaxies are almost equally divided between a BLAGN SED class (similar to an optically selected QSO) and a NLAGN SED (similar to the BLAGN SED but with an obscured UV/optical continuum). A small fraction of SEDs resemble warm ULIRG galaxies (e.g., Mrk 231). Most galaxies not detected in X-rays have SEDs in the NLAGN+ULIRG class as they tend to be optically fainter, and possibly more obscured. Moreover, the IR power-law galaxies have SEDs significantly different from those of high- z ($z_{\text{sp}} > 1$) IR ($24\mu\text{m}$) selected and optically bright (VVDS $I_{\text{AB}} \leq 24$) star-forming galaxies

¹Departamento de Astrofísica Molecular e Infrarroja, Instituto de Estructura de la Materia, CSIC, E-28006 Madrid, Spain; e-mail: aalonso@damir.iem.csic.es

²Steward Observatory, The University of Arizona, 933 N. Cherry, Tucson, AZ 85721

³Institute of Astronomy, University of Cambridge, Madingley Road, Cambridge, CB3 0HA, UK

⁴Department of Astrophysics, Oxford University, Keble Rd, Oxford, OX1 3RH, UK

⁵Harvard-Smithsonian Center for Astrophysics, Cambridge, MA 02138

⁶Columbia Astrophysics Laboratory, Columbia University Pupin Laboratories, 550 W. 120th St., Rm 1418, NY, 10027

⁷Department of Astronomy and Astrophysics; The Pennsylvania State University; 525 Davey Lab; University Park, PA 16802

⁸Institut d'Astrophysique Spatiale, bât 121, Université Paris Sud, F-91405 Orsay Cedex, France

whose SEDs show a very prominent stellar bump at $1.6 \mu\text{m}$. The galaxies detected in X-rays have $2 - 8 \text{ keV}$ rest-frame luminosities typical of AGN. The galaxies not detected in X-rays have global X-ray to mid-IR SED properties that make them good candidates to contain IR bright X-ray absorbed AGN. If all these sources are actually obscured AGN, we would observe a ratio of obscured to unobscured $24 \mu\text{m}$ detected AGN of 2:1, whereas models predict a ratio of up to 3:1. Additional studies using *Spitzer* to detect X-ray-quiet AGN are likely to find more such obscured sources.

Subject headings: Infrared: galaxies — X-rays: galaxies — galaxies: active

1. Introduction

Active galactic nuclei (AGN) are sources of luminous X-ray emission, and at cosmological distances AGN are routinely selected from deep X-ray ($< 10 \text{ keV}$, *Chandra* and *Newton-XMM*) exposures (see Brandt & Hasinger 2005 for a recent review). However, obscured (Compton thick) AGN are thought to be a major contributor to the hard X-ray background (Comastri et al. 1995) and the majority of them might not be detected in these X-ray surveys. Since a large fraction of their soft X-ray, UV and optical emission is absorbed, and presumably reradiated in the infrared (IR), obscured AGN are also believed to make a significant contribution to the IR and submillimeter backgrounds (Fabian & Iwasawa 1999; Almaini, Lawrence, & Boyle 1999). Fadda et al. (2002) used ISOCAM on the *Infrared Space Observatory (ISO)* in X-ray survey fields to estimate that X-ray emitting AGN contribute up to 17% of the $15 \mu\text{m}$ extragalactic background (see also Alexander et al. 2002; Silva, Maiolino, & Granato 2004).

Since their discovery, it has been recognized that the UV and optical continuum of luminous QSOs could be described with a power law that can continue all the way into the near, mid, and even far-IR (see e.g., Neugebauer et al. 1979; Elvis et al. 1994). This behavior often arises from the combination of a number of source components that broaden the purely stellar spectral energy distribution (SED), rather than from a dominant contribution from a true power-law source (see, e.g., Rieke & Lebofsky 1981). Nonetheless, it is a surprisingly general characteristic. At lower luminosities, for instance X-ray selected Seyfert 1 galaxies, the most common SED from the UV to the far-IR is a relatively flat νf_ν distribution, although for some of the sources the observed SEDs show the effects of dust obscuration and thermal emission (e.g., Ward et al. 1987; Carleton et al. 1987). A similar result is found for optically selected Seyfert galaxies in the CfA sample, although Seyfert 2 galaxies tend to have steeper IR slopes, probably due to the effects of dust emission/obscuration (e.g., Edelson, Malkan,

& Rieke 1987). Optical and IR power-law emission is also present in X-ray selected QSOs (HEAO, Kuraszkiewicz et al. 2003) and near-IR selected QSOs (2MASS, Wilkes et al. 2005).

Therefore, sensitive measurements in the IR range provide an opportunity to look for obscured AGN not identified in X-ray and optical surveys. First, unlike normal and star forming galaxies whose near-IR SEDs are dominated by the $1.6\ \mu\text{m}$ stellar bump, AGN dominated galaxies (even those obscured at optical wavelengths) could be potentially identified through power-law emission in the rest-frame near-IR ($1 - 5\ \mu\text{m}$). For instance, Egami et al. (2004) have found SCUBA/VLA sources not detected in X-rays whose SEDs show a power-law shape, and probably contain an AGN. Second, Alexander et al. (2005) have shown that among the most IR-luminous high- z galaxies — those detected at high redshift with SCUBA — the AGN fraction is high, at least 40%, suggesting that the most IR-luminous high- z galaxies may be good candidates to host AGN. Very recent *Spitzer* spectroscopy of IR luminous galaxies at $z \simeq 1 - 2$ has shown a similar fraction of galaxies containing an AGN (Yan et al. 2005).

In this paper we investigate the nature of galaxies selected at the *Spitzer*/MIPS $24\ \mu\text{m}$ band and within the *Chandra* Deep Field South (CDFS), and that show power-law-like emission in the *Spitzer*/IRAC $3.6 - 8\ \mu\text{m}$ bands. By selecting galaxies at $24\ \mu\text{m}$ we ensure that at $z > 1$ a large fraction of them will be in the ultraluminous IR galaxy (ULIRG, $L_{\text{IR}} > 10^{12} L_{\odot}^1$) class (see Pérez-González et al. 2005). Throughout this paper we use $H_0 = 71\ \text{km s}^{-1} \text{Mpc}^{-1}$, $\Omega_{\text{M}} = 0.3$, and $\Omega_{\Lambda} = 0.7$.

2. Spitzer Observations

We have obtained $24\ \mu\text{m}$ and $70\ \mu\text{m}$ MIPS (Rieke et al. 2004) observations of the CDFS covering a total area of $1.5\ \text{deg} \times 0.5\ \text{deg}$. In this work we will only focus on the field of view (FOV) with *Chandra* coverage ($\simeq 390\ \text{sqr arcmin}$, Giacconi et al. 2002; Alexander et al. 2003a). The MIPS data were reduced using the Data Analysis Tool (DAT) package developed by the MIPS instrument team (Gordon et al. 2005).

The $24\ \mu\text{m}$ source detection and photometry, described in detail by Papovich et al. (2004) and Pérez-González et al. (2005), assumed that all sources were point-like, given the $\simeq 5.8''$ FWHM angular resolution. PSF-fitting with DAOPHOT (Stetson 1987) packages *daofind*, *phot*, and *allstar* in IRAF gave positions, fluxes, and uncertainty estimates. The final 5σ flux density limit was $83\ \mu\text{Jy}$ and the catalog is 80% complete at this level (see Papovich

¹The IR luminosities are in the $8 - 1000\ \mu\text{m}$ range (Sanders & Mirabel 1996).

et al. 2004). We measured photometry at $70\ \mu\text{m}$ using the $24\ \mu\text{m}$ positions as a priori information. We used a version of the DAOPHOT/ALLFRAME package (Stetson 1994), which simultaneously fits the $70\ \mu\text{m}$ PSF at the position of each $24\ \mu\text{m}$ source in the $70\ \mu\text{m}$ image for sources within $50''$ of nearby object centroids. This method has the advantage of recovering photometry from faint sources in the $70\ \mu\text{m}$ image, even when sources are partially confused. The errors on the $70\ \mu\text{m}$ sources include an uncertainty on the fitting of sources with overlapping isophotes, providing an estimate of the error on each source owing any source confusion. The DAOPHOT/ALLSTAR PSF-fitting software detected $70\ \mu\text{m}$ sources down to an upper limit of $3\ \text{mJy}$, fainter than that of Dole et al. (2004) because of the use of the $24\ \mu\text{m}$ a priori information.

The CDFS was observed by IRAC (Fazio et al. 2004) at 3.6 , 4.5 , 5.8 , and $8\ \mu\text{m}$ covering an area of $1.0\ \text{deg} \times 0.5\ \text{deg}$. IRAC photometry began with the Basic Calibrated Data images from the *Spitzer* Science Center pipeline, version 9.5. Custom IDL software projected the individual frames onto a uniform grid of $0''.6$ pixels, conserving flux and rejecting outliers such as cosmic ray hits. Source detection and photometry were carried out with SEXTRACTOR (Bertin & Arnouts 1996). We used a small circular aperture ($3''$ in diameter) and an aperture correction to get the total flux (assumed to be the one corresponding to a circular aperture of diameter $24.4''$) of each source. The aperture corrections were calculated from in-flight PSFs. This procedure is similar to that used by Huang et al. (2004). The photometry errors take into account the IRAC photometric calibration uncertainty and the SEXTRACTOR photometry errors.

3. Selection of IR power-law galaxies

Galaxies dominated by AGN emission typically show a power law ($f_\nu \propto \nu^\alpha$, where α is the spectral index) SED at rest-frame optical, near- and mid-IR wavelengths, though with a variety of slopes. Elvis et al. (1994) showed that optically selected QSOs have average optical to IR spectral indices around $\alpha = -1$ (see also Neugebauer et al. 1979). More recent results from the Sloan Digital Sky Survey (SDSS) show that the optical spectral indices of optically selected QSOs are in the range of $\alpha = -0.5$ to -2 (Ivezić et al. 2002, their figure 17). Of course this does not necessarily mean that the spectral index is the same in the near- and mid-IR. 2MASS QSOs also show power-law-like SEDs in the near- and mid-IR, very similar to those of optically selected QSOs, although the UV-optical continuum shape is steeper than that of optically and X-ray selected QSOs (Wilkes et al. 2005). ULIRGs ($L_{\text{IR}} > 10^{12}\ L_\odot$) containing an AGN, in particular warm ULIRGs, also have near and mid-IR SEDs resembling power laws (see Sanders et al. 1988, and more recently Klaas et al. 2001).

Some of these warm ULIRGs in the local Universe are also identified with optically selected QSOs, and all of them are known to host an AGN. Moreover, warm ULIRGs have been proposed as an intermediate stage in the evolution between ULIRGs and QSOs (Sanders et al. 1988; Sanders et al. 2004, and references therein). Thus the presence of an IR power law in LIRGs and ULIRGs could also be an indication of the presence of an AGN.

To construct an initial power-law galaxy sample, we started with the $24\ \mu\text{m}$ source catalog (Papovich et al. 2004) in the FOV of the X-ray *Chandra* observations of the CDFS. We cross-correlated the positions of these $24\ \mu\text{m}$ sources with sources detected in the four IRAC bands using a $1.5''$ search radius, and constructed observed $3.5 - 8\ \mu\text{m}$ SEDs, requiring that the sources be detected in all four IRAC bands. We fitted the SEDs with a power law $f_\nu \propto \nu^\alpha$ between 3.6 and $8\ \mu\text{m}$, and minimized χ^2 to select galaxies whose IRAC SEDs followed a power law with spectral index $\alpha < -0.5$. These objects formed the candidate list for our sample, subject to construction of full SEDs toward shorter wavelengths. Further tests of the power-law nature of these objects were used to derive the final sample, as described in the Appendix.

Recently Lacy et al. (2004) and Stern et al. (2005) have used IRAC observations of SDSS QSOs in the *Spitzer* First Look Survey and spectroscopically confirmed AGN in the Boötes Field respectively, to derive an empirical color selection for AGN. They show that bright QSOs and broad-line AGN occupy a very distinct region in the IRAC color-color diagram. Follow-up optical spectroscopy of some of the optically faint AGN candidates identified by Lacy et al. (2004) show high ionization narrow lines typical of obscured type 2 AGN (see Lacy et al. 2005) demonstrating the effectiveness of this method. We note that our criteria select galaxies along a line in the IRAC color-color diagram, rather than using the full region identified by Lacy et al. 2004 (their figure 1). Our approach is therefore more restrictive than theirs, since we depend entirely on the SED behavior to identify candidate AGN. Barmby et al. (2005) present a detailed comparison between the IRAC power-law and the IRAC color-color selection methods for AGN in the Extended Groth Strip.

The final sample consists of 92 galaxies referred to here as “IR power-law galaxies”. They have been selected without regard to X-ray properties, and should be unbiased in that respect, and can therefore be used to probe the number of X-ray quiet AGN in the CDFS. Thirty-seven members of the sample are also detected with MIPS at $70\ \mu\text{m}$ down to a limit of $f_{70\ \mu\text{m}} \simeq 3\ \text{mJy}$. Table 1 gives *Spitzer* coordinates, flux densities and uncertainties, as well as the fitted IRAC spectral indices α for the sample of IR power-law galaxies.

An interesting aspect of these galaxies is that we found a maximally steep optical-to-IR slope corresponding to $\alpha \sim -2.8$ (see Table 1). A similar limit was found by Rigby et al. (2005a) in studying a complete sample of optically faint X-ray sources in the CDFS. Stickel

et al. (1996) studied a complete sample of faint identifications of flat spectrum radio sources. They also found that the steepest optical-IR SEDs were characterized by $\alpha \sim -2.5$. This slope therefore seems to define a limiting behavior for AGN SEDs.

4. X-ray Observations

The CDFS field has ultra-deep 1 Ms *Chandra* observations (Giacconi et al. 2002 and Alexander et al. 2003a), providing a sensitive census of AGN activity. The aim-point sensitivities in the 0.5 – 8.0 keV (full), 0.5 – 2.0 keV (soft), and 2 – 8 keV (hard) bands are $\approx 1.3 \times 10^{-16}$ erg cm $^{-2}$ s $^{-1}$, $\approx 5.2 \times 10^{-17}$ erg cm $^{-2}$ s $^{-1}$, and $\approx 2.8 \times 10^{-16}$ erg cm $^{-2}$ s $^{-1}$, respectively. As an example, assuming an X-ray spectral slope of $\Gamma = 2.0$, a source detected with a flux of $\approx 1.0 \times 10^{-16}$ erg cm $^{-2}$ s $^{-1}$ would have both observed and rest-frame luminosities of $\approx 5.8 \times 10^{41}$ erg s $^{-1}$, $\approx 8.4 \times 10^{42}$ erg s $^{-1}$, and $\approx 2.8 \times 10^{43}$ erg s $^{-1}$ at $z = 1$, $z = 3$, and $z = 5$, respectively.

The majority of the X-ray data are taken from tables 3a and 3b of the main catalog of Alexander et al. (2003a). However, for the faintest X-ray sources, the data were taken from a largely unpublished supplementary catalog. We cross-correlated the positions of our 92 IR power-law SED galaxies with the X-ray sources using a 1.2 – 3'' search radius, with the latter for X-ray sources at large off-axis angles. Apart from the sources in common with the Alexander et al. (2003a) catalog, there is a further source in the Giacconi et al. (2002) catalog. For this source we converted the 2 – 10 keV band to the 2 – 8 keV and 0.5 – 8 keV bands assuming $\Gamma = 1.4$. We found that 49 galaxies are detected at least in one of the *Chandra* bands, whereas 43 galaxies (47%) are not detected in any of the *Chandra* bands. For the X-ray undetected sources we calculated 3σ upper limits (assuming $\Gamma = 1.4$) in the full, soft, and hard bands following Alexander et al. (2003a). The X-ray information on the IR power-law galaxy sample is given in Table 2, including the off-axis angle that shows the sensitivity variation across the X-ray field. At off-axis angles of less than 9' (where the sensitivity is more uniform), the fraction of sources not detected at any *Chandra* band is 41%.

Fig. 1 compares the X-ray and mid-IR emission of the CDFS galaxies detected both at 24 μ m and in hard X-rays (filled dots) from Alonso-Herrero et al. (2004) and Rigby et al. (2004), and among them those identified as IR power-law SED galaxies (squares). The IR power-law SED galaxies comprise about one third of all the hard X-ray sources with 24 μ m detections. We also show those IR power-law SED galaxies with only upper limits in the *Chandra* hard X-ray band (2 – 8 keV). The IR and X-ray properties of our sample will be discussed in more detail in §6 and §7, respectively.

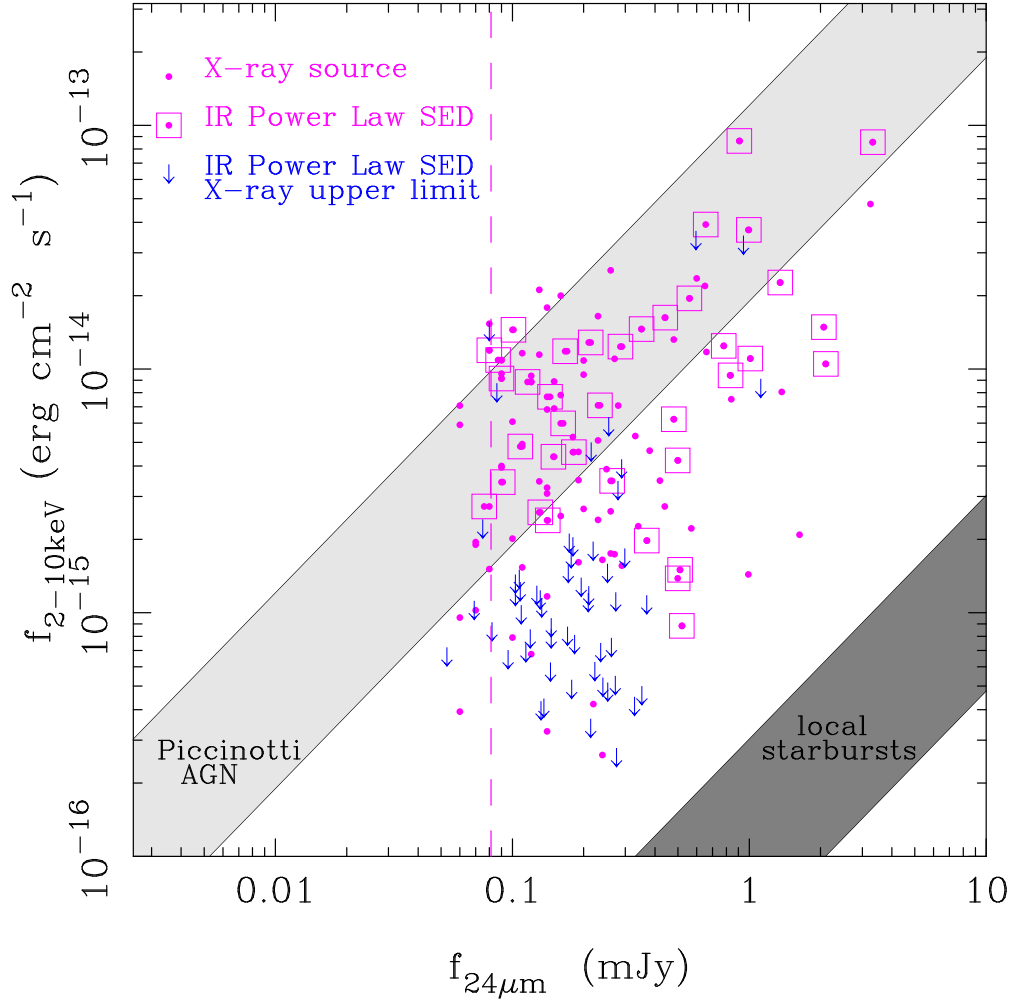


Fig. 1.— $24\mu\text{m}$ fluxes vs. $2 - 10\text{ keV}$ X-ray fluxes of X-ray selected sources with $24\mu\text{m}$ counterparts in the CDFS (dots, see Rigby et al. 2004); those also marked with a square symbol are IR power-law SED galaxies in our sample. Those IR power-law SED galaxies in our sample not detected in hard X-rays are shown as upper limits (arrows). The *Chandra* $2 - 8\text{ keV}$ fluxes have been converted to $2 - 10\text{ keV}$ fluxes assuming a power law with photon index $\Gamma = 1.4$, for easy comparison with figure 1 in Alonso-Herrero et al. (2004). The dashed line is the 80% completeness limit for the CDFS $24\mu\text{m}$ source catalog (Papovich et al. 2004). The lightly shaded area is the extrapolation of the median hard X-ray to mid-IR ratios ($\pm 1\sigma$) of local ($z < 0.12$) hard X-ray selected AGN (Piccinotti et al. 1982) with mid-IR emission. The dark shaded area is the extrapolation of local starburst galaxies from Ranalli, Comastri, & Setti (2003).

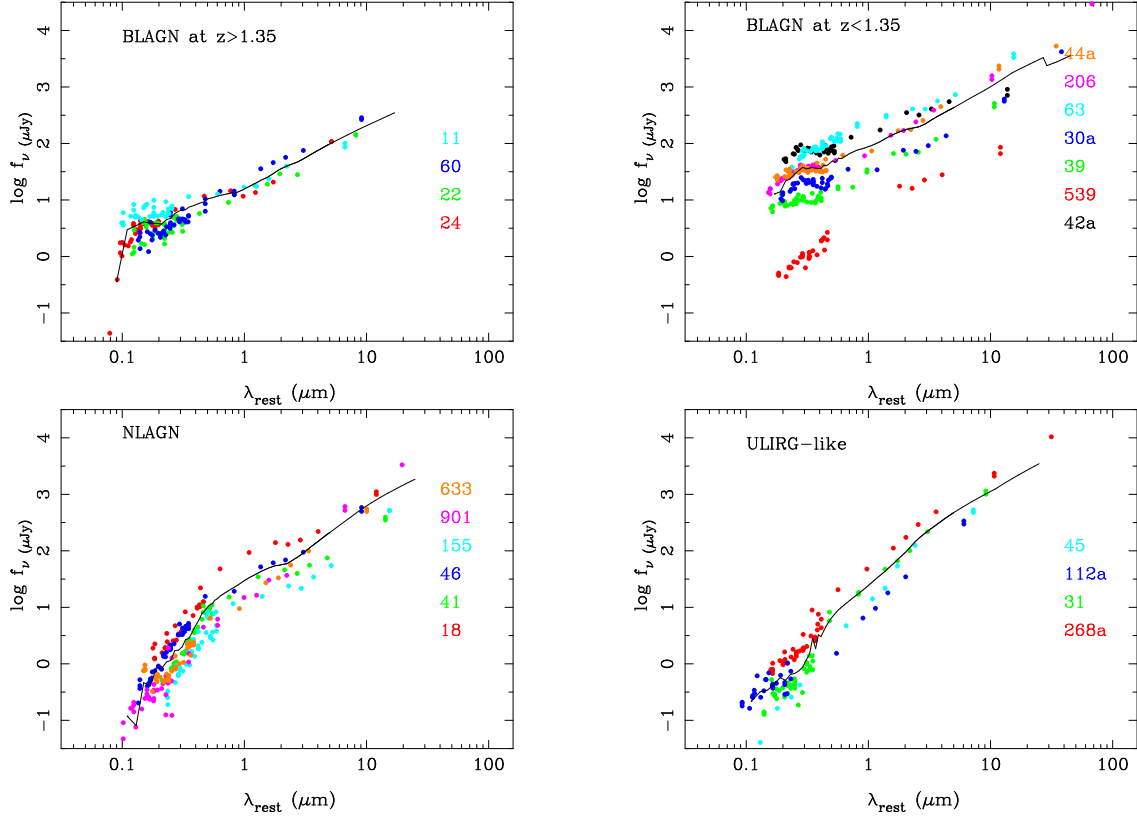


Fig. 2.— Rest-frame SEDs (dots) of IR power-law galaxies detected in X-rays for 21 galaxies with spectroscopic redshifts available from the Szokoly et al. (2004) sample. The galaxy names shown on the right hand side of each panel refer to source IDs in Szokoly et al. (2004). For each type of galaxy we have constructed an average template, shown as the solid line in each panel.

5. Spectral Energy Distributions of IR power-law galaxies

5.1. X-ray detected galaxies with spectroscopic redshifts

We cross-correlated our sample against the spectroscopic redshift catalogs of Szokoly et al. (2004) and the VIRMOS-VLT Deep Survey (VVDS, Le Fèvre et al. 2004) for CDFS galaxies. Twenty-three IR power-law galaxies detected in X-rays have spectroscopic redshifts, of which twenty-two are in the Szokoly et al. (2004) sample and thus an activity class based on emission lines is also available. The Szokoly et al. (2004) activity classes are: broad-line AGN (BLAGN), high excitation line galaxies (HEX), and low excitation line galaxies (LEX).

We can use the Szokoly et al. (2004) measurements to determine the efficiency of our criterion in finding X-ray QSOs. Of the twenty-nine CDFS sources classified as X-ray QSOs ($L_{0.5-10\text{keV}} > 10^{44} \text{ erg s}^{-1}$) by Szokoly et al. (2004), twenty-three are detected at $24 \mu\text{m}$. Our IR power-law criteria identifies eleven out of the fourteen broad-line QSOs, plus two narrow-line unabsorbed QSOs. Out of the nine X-ray type-2 QSOs in Szokoly et al. (2004) detected at $24 \mu\text{m}$, we only select three as IR power-law galaxies. Of the six X-ray type-2 QSOs not identified with our sample selection criteria, three are missing an IRAC band, and the other three do not show a power-law SED (i.e., they appear dominated by stellar emission).

There are six further IR power-law galaxies in common with the Szokoly et al. (2004) sample. They are classified as AGN in terms of their X-ray luminosities ($L_{0.5-10\text{keV}} = 10^{42} - 10^{44} \text{ erg s}^{-1}$), with two broad-line AGN, and the other four with narrow lines (HEX and LEX classes). We note that there are no galaxies with absorption lines (the ABS class of Szokoly et al. 2004) included in our sample of IR power-law galaxies, as those galaxies tend to be dominated by stellar emission (Rigby et al. 2005b).

In Fig. 2 we show the rest-frame SEDs of the galaxies in our sample detected in X-rays and with spectroscopic redshifts. We define three SED categories:

- The broad-line AGN (BLAGN) SED category includes galaxies whose SEDs resemble those of optically selected QSOs, such as the median QSO of Elvis et al. (1994), and of X-ray selected QSOs (Kuraszkiewicz et al. 2003) — that is, galaxies with an optical to mid-IR continuum almost flat in νf_ν with a UV bump. All but one of the galaxies in the BLAGN SED category are X-ray QSOs in terms of their X-ray luminosities (Szokoly et al. 2004), and all of them show broad lines. We have further divided the BLAGN galaxies in our sample into two arbitrary redshift intervals to determine if there are significant differences in their SEDs.
- The second SED class consists of galaxies with IR SEDs similar to the BLAGN SED

galaxies but whose UV and optical continua are much steeper (obscured) and resemble the SEDs of 2MASS QSOs (Wilkes et al. 2005). The galaxies will be referred to as narrow line AGN (NLAGN) since in terms of the optical spectroscopic classification most of these galaxies do not show broad lines. Using the classifications of Szokoly et al. (2004), we find three HEX galaxies, two LEX galaxies, and one BLAGN.

- The last SED class is for galaxies with the steepest IR SEDs, resembling that of the local warm ULIRG Mrk 231 (see Fig. 2). Although there is no formal division between this SED class and the NLAGN SED class, the ULIRG SED galaxies do not show a prominent $1.6\ \mu\text{m}$ stellar bump. In terms of their X-ray luminosities, three are classified by Szokoly et al. (2004) as QSOs, and the other one is a type 2 AGN. In terms of their spectroscopic classification (Szokoly et al. 2004), there are three HEX galaxies and one LEX galaxy.

For each of the SED classes defined above, we have constructed typical SEDs that can be used as templates to classify the galaxies. These templates used a number of techniques such as averaging the observations of a number of galaxies to increase the signal and to smooth over individual eccentricities. As Fig. 2 shows, the templates match the observations of individual galaxies well. We note that the stellar bump at $1.6\ \mu\text{m}$ is present, although it is not very prominent, on the average templates of NLAGN and low- z BLAGN. The average templates of the high and low- z BLAGN SED are very similar except that in the high- z BLAGN AGN the $1.6\ \mu\text{m}$ stellar bump seems to be absent (note however, that only four galaxies were used to construct this average template).

5.2. X-ray detected galaxies with photometric redshifts

For galaxies showing SEDs resembling the BLAGN SED category, virtually all of which are known X-ray sources, we use mostly phot- z estimates from COMBO-17 and Zheng et al. (2004). Where redshifts are not available from the literature, we determined redshifts with the code discussed by Pérez-González et al. (2005). Briefly, the code uses the observed optical to mid-IR SEDs and a full set of empirically determined and theoretical templates (such as those in Fig. 2) to derive phot- z 's. As discussed by Pérez-González et al. (2005), the main advantage of our phot- z code when used with optical to mid-IR SEDs is the possibility of using the $1.6\ \mu\text{m}$ bump in addition to the optical stellar features routinely employed by other phot- z codes. For galaxies with such a bump, Pérez-González et al. (2005) demonstrate that the code gives reliable redshifts out to $z \sim 3$ (compare also with the results of Caputi et al. 2005, which confirm the general results obtained with our code).

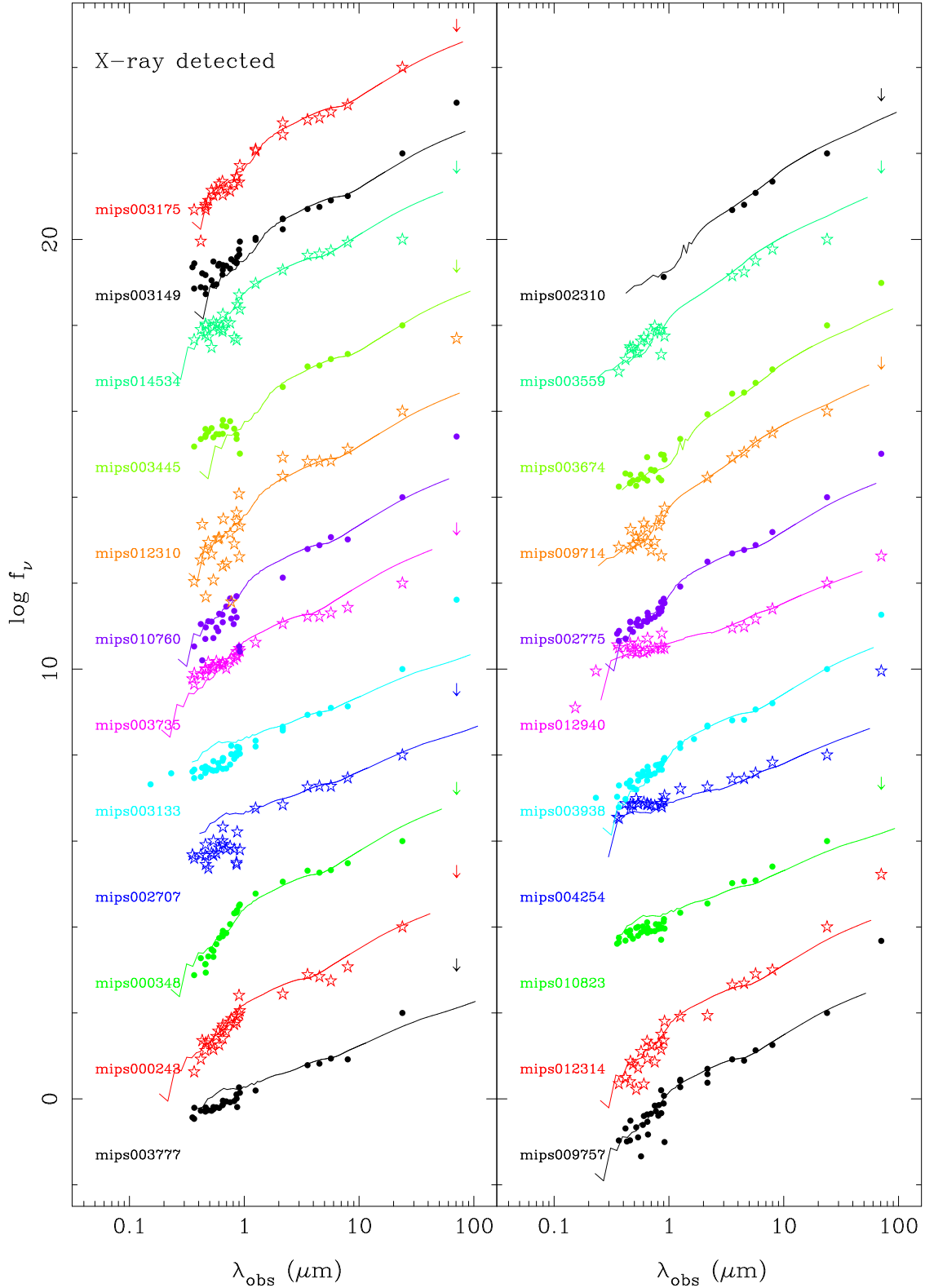


Fig. 3.— Observed SEDs, arbitrarily offset for clarity, (filled dots and star symbols) of IR power-law galaxies detected in X-rays for which spectroscopic redshifts are not available. Each galaxy is shown with the closest matching SED template from those shown in Fig. 2 redshifted to the phot-z estimate. Note that this SED template is not the template used for computing the phot-z, and is only used for source classification purposes (see text for more

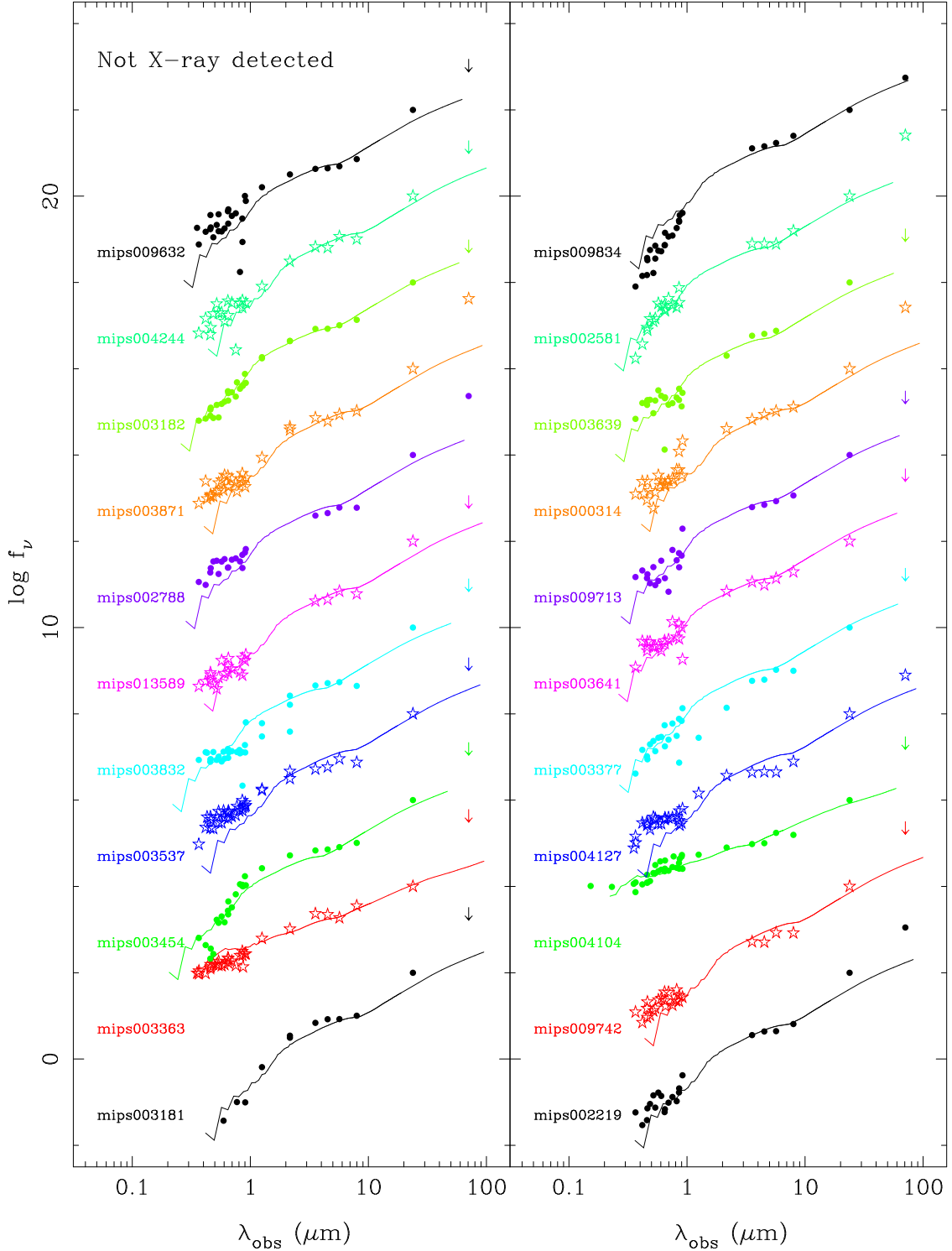


Fig. 4.— Observed SEDs, arbitrarily offset for clarity, (filled dots and star symbols) of IR power-law galaxies not detected in X-rays for which spectroscopic redshifts are not available. Each galaxy is shown with the closest matching SED template from those shown in Fig. 2 redshifted to the phot-z estimate. Note that this SED template is not the template used for computing the phot-z, and is only used for source classification purposes (see text for more details). For those galaxies not detected with MIPS at $70 \mu\text{m}$ the upper limits are set to the detection limit of $f_{70 \mu\text{m}} \simeq 3 \text{ mJy}$.

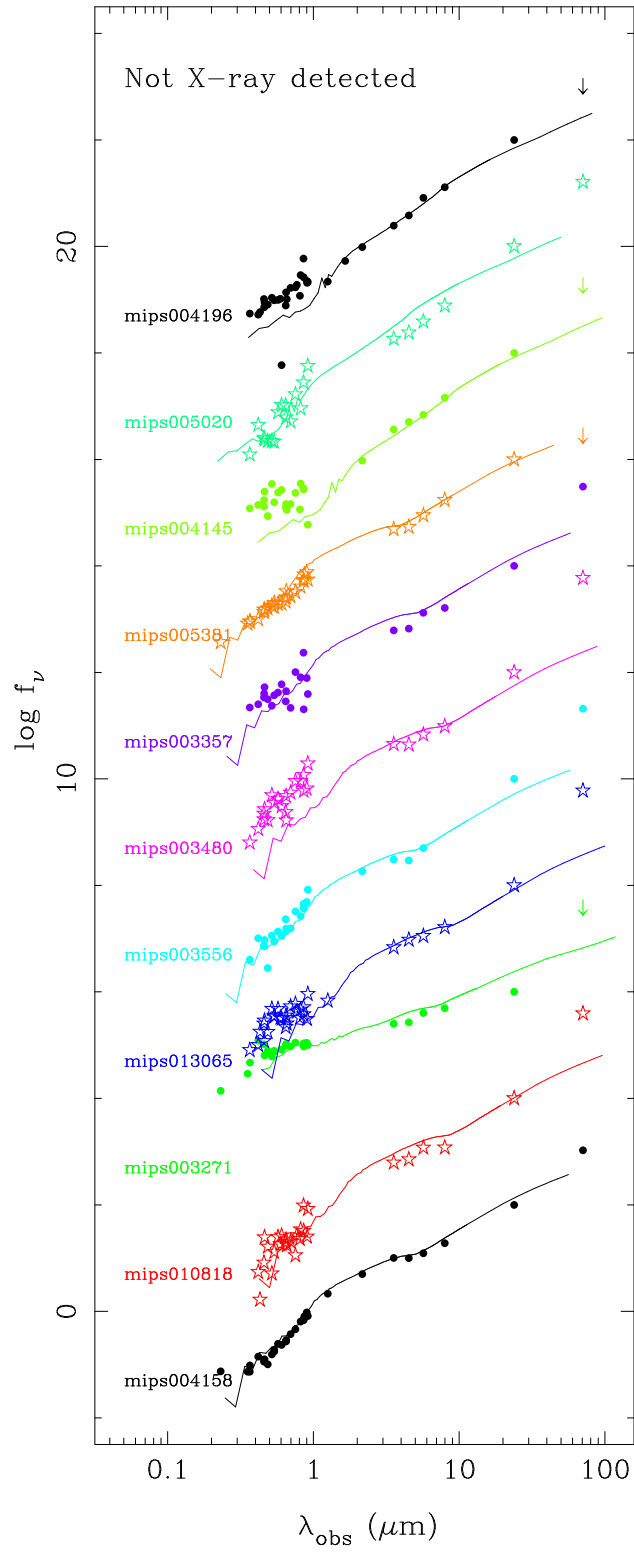


Fig. 4.— Continued.

However, many of our sources do not have a prominent $1.6\ \mu\text{m}$ bump. Rigby et al. (2005a) used the same code to estimate redshifts for optically faint AGN, a substantially more difficult problem than even the sources in our program. They found that the values returned were in good agreement both with redshifts from the literature, when available, and with those estimated by eye. In particular, although they found a large range of permissible redshifts for their sources, an equivalent range in our estimates would not affect our conclusions.

Both Pérez-González et al. (2005) and Rigby et al. (2005a) find difficulty in getting redshifts for purely power-law SEDs. Fortunately, most such objects in our sample are in the BLAGN group and redshifts are available from the literature based on other redshift determined techniques. The great majority of sources without redshifts depart from the power-law behavior at short wavelengths, and hence have features or a general shape that allows the phot-z code to return a value. To test the reliability of these values, we have cross-correlated our sample with the phot-z catalog of Zheng et al. (2004), with COMBO-17 (Wolf et al. 2004), and for the objects with spectroscopic redshifts, and we find good agreement for galaxies whose SEDs resemble the NLAGN template. Since we use the redshifts only for rough estimates of luminosities (§6.1 and 7), precise values are not required and we find that the phot-z’s are sufficiently accurate for our purposes.

Fig. 3 shows the observed SEDs for twenty-three out of the twenty-six galaxies in our sample detected in X-rays without spectroscopic redshifts; the three galaxies not shown here have few points in their SEDs and an estimate of their phot-z was not possible. We do not use the templates obtained in this work for phot-z determination because of possible interactions between the redshift and the type determination for the SED. Our phot-z code instead uses actual SEDs of observed galaxies (see Pérez-González et al. 2005 for a full description). The SEDs of the majority of the IR power-law galaxies in Fig. 3 (see also §5.3, and Fig. 4) match one of the three SED categories defined in §5.1. For each galaxy in Fig. 3 we plot the closest matching average template defined in this work, not constrained to be the template used by our phot-z code, redshifted to the estimate of phot-z. The average SED templates are only used for source classification purposes, and to estimate the rest-frame $12\ \mu\text{m}$ flux density from the observed $24\ \mu\text{m}$ value (see §6.1). The galaxies are shown in approximate order of increasing IRAC slopes. The estimated phot-z’s are between 0.7 and 2.8. Most of the galaxies without spectroscopic redshifts show SEDs similar to the NLAGN template as they tend to be optically fainter than those with spectroscopic redshifts. A few galaxies with very steep IRAC slopes resemble the local ULIRG Mrk 231.

5.3. Galaxies not detected in X-rays

Among the galaxies not detected in X-rays, we have only found one galaxy in the VVDS spectroscopic redshift sample (Le Fèvre et al. 2004). For the rest of the galaxies not detected in X-rays we have estimated phot- z 's and analyzed the SEDs using the same technique as in §5.2. Fig. 4 shows the SEDs (in order of increasing IRAC slope) for the 32 IR power-law galaxies not detected in X-rays for which we could estimate phot- z 's plus the galaxy with the VVDS spectroscopic redshift; the other 10 sources have incomplete SEDs and a reliable estimate of the phot- z was not possible.

The majority of these sources have SEDs similar to the NLAGN template; a few show very steep SEDs similar to that of Mrk 231. Only three galaxies show an SED similar to that of a BLAGN. One of these sources (mips003271) is classified by COMBO-17 as a QSO based on the presence of broad lines with a phot- z of $z_{\text{COMBO}} = 1.63$. This galaxy is located at a large X-ray off-axis angle in the *Chandra* images (see Table 2) where the X-ray sensitivity is less, and the upper limit to its X-ray luminosity is consistent with the presence of an AGN. The second source (mips004104) appears to be a relatively nearby galaxy ($z_{\text{COMBO}} = 0.31$), but its SED is similar to that of a broad line AGN. The third source (mips003363) has a COMBO-17 phot- z of $z_{\text{COMBO}} = 1.2$, and is also located at a large off-axis angle. The phot- z 's of the IR power-law galaxies not detected in X-rays are between 0.3 and 3 (see insert of Fig. 5).

5.4. Summary of properties

The SEDs of IR power-law galaxies detected in X-rays are approximately equally divided between the BLAGN SED category (40%) and NLAGN+ULIRG SED category (60%). As the division between the NLAGN and the ULIRG SED category is rather arbitrary, in what follows we discuss both categories jointly. The galaxies not detected in X-rays are mostly in the NLAGN+ULIRG SED category, consistent with the fact that the majority of these galaxies are optically faint — most have COMBO-17 R -band magnitudes $R > 24$ mag (see Appendix) — and are possibly more obscured than the X-ray detected ones. The distribution of $24\ \mu\text{m}$ flux densities near the completeness limit, on the other hand, is similar for galaxies detected and not detected in X-rays (see Fig. 1). Both the galaxies detected in X-rays and those not detected in X-rays show a similar fraction of $70\ \mu\text{m}$ detections ($\simeq 40\%$) down to an approximate limit of $f_{70\ \mu\text{m}} \simeq 3\ \text{mJy}$ (see Table 1).

In terms of the redshift distribution (see insert of Fig. 5) the majority of the IR power-law galaxies (both those detected in X-rays and those not detected in X-rays) appear to

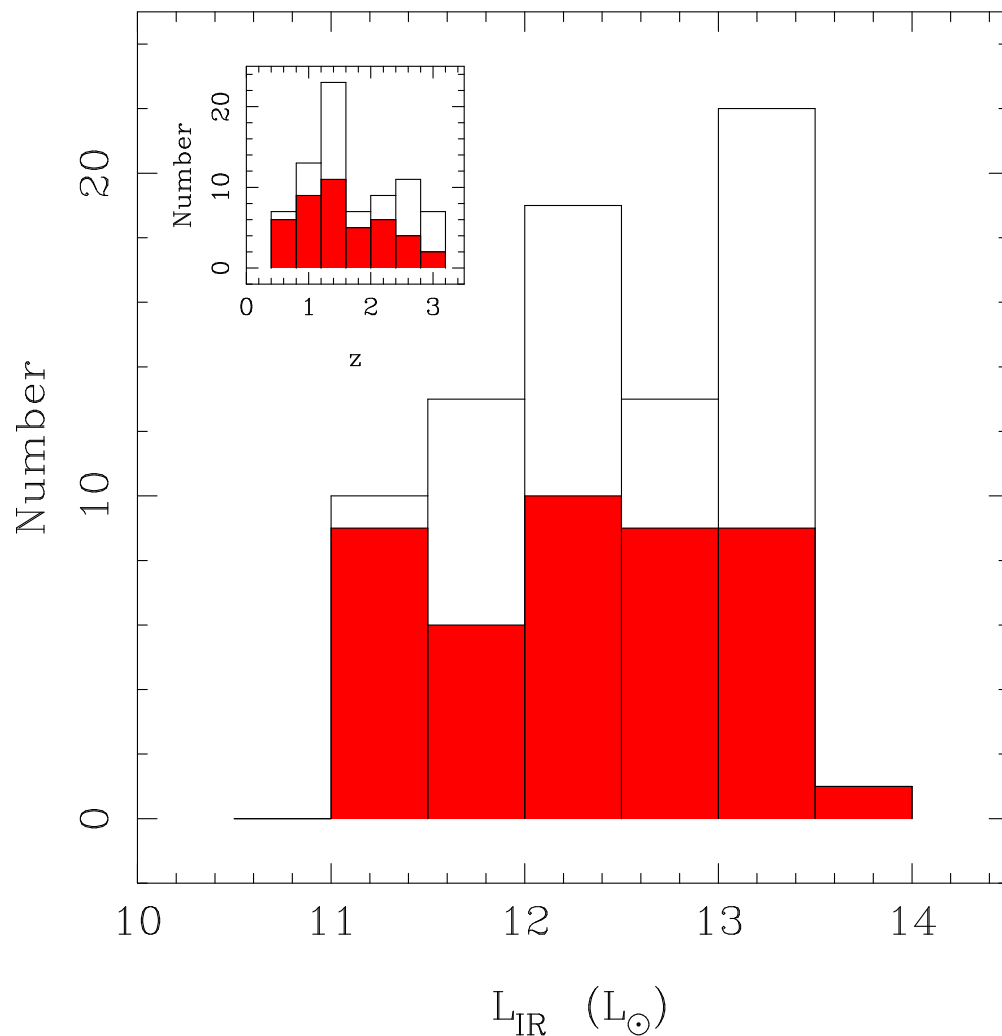


Fig. 5.— *Main panel:* Distribution of the rest-frame IR 8 – 1000 μm luminosity for the entire sample of IR power-law galaxies with redshifts (empty histogram) and those detected in X-rays (filled histogram). *Insert:* Distribution of redshifts (both spectroscopic and photometric) of the IR power-law galaxies (empty histogram), and the galaxies detected in X-rays (filled histogram).

be at $z > 1$. This is in contrast with the two observed peaks in the spectroscopic redshift distribution of the X-ray sources in the CDFS ($z = 0.674$ and $z = 0.734$, Szokoly et al. 2004) and the spectroscopic redshift grouping of galaxies with $I_{\text{AB}} \leq 24$ observed by VVDS ($z = 0.73$, Le Fèvre et al. 2004). There seems to be a slightly larger proportion of IR power-law galaxies at $z > 2$ not detected in X-rays (15 out of 33) than detected in X-rays (12 out of 46), but this result needs to be confirmed spectroscopically. Most of the IR power-law galaxies at $z < 1$ are detected in X-rays.

6. Infrared properties

6.1. Rest-frame $12\ \mu\text{m}$ and Total IR Luminosities

While the total IR ($8 - 1000\ \mu\text{m}$) luminosity cannot be measured directly for most of the IR power-law galaxies in our sample, a number of works (e.g., Rush, Malkan, & Spinoglio 1993; Spinoglio et al. 1995; Takeuchi et al. 2005; Pérez-González et al. 2005) have shown that the $12\ \mu\text{m}$ luminosity is a good proxy for it for AGNs, LIRGs, and ULIRGs.

We have computed the $12\ \mu\text{m}$ to IR luminosity conversion factors from warm ($f_{25\ \mu\text{m}}/f_{60\ \mu\text{m}} > 0.2$) and cool ($f_{25\ \mu\text{m}}/f_{60\ \mu\text{m}} < 0.2$, see Sanders & Mirabel 1996) ULIRGs in the local Universe (those discussed in Appendix A.3) to be used for IR power-law galaxies in the BLAGN and NLAGN+ULIRG SED classes, respectively. Although our procedure to compute IR luminosities is very similar to that used by Pérez-González et al. (2005), we have taken special care to use $12\ \mu\text{m}$ to IR luminosity ratios specific to the class of galaxies in study. In particular, galaxies whose SEDs resemble those of optical QSOs show $12\ \mu\text{m}$ to IR luminosity ratios significantly lower than the typical values of cool ULIRGs and some warm ULIRGs (e.g., Mrk 231). The $12\ \mu\text{m}$ rest-frame luminosities are derived from the observed $24\ \mu\text{m}$ values using the spectral indices of power laws fitted in the $\lambda_{\text{rest}} = 10 - 30\ \mu\text{m}$ range of the average templates defined in §5.1. The IR luminosities are only computed for those galaxies with spectroscopic redshifts and reliable estimates of the phot- z .

All the IR power-law galaxies are highly luminous. About 30% are in the hyperluminous class ($L_{\text{IR}} > 10^{13}\ L_{\odot}$; Kleinmann et al. 1989, and see also Rowan-Robinson 2000), 41% are ULIRGs ($L_{\text{IR}} = 10^{12} - 10^{13}\ L_{\odot}$), and all but one of the rest are LIRGs ($L_{\text{IR}} = 10^{11} - 10^{12}\ L_{\odot}$). Fig. 5 shows the distribution of IR luminosities. At the lower IR luminosity end ($L_{\text{IR}} < 10^{12}\ L_{\odot}$) a large fraction are detected in X-rays and are mostly in the BLAGN SED category. The fraction of X-ray detected galaxies in the sample of IR power-law galaxies remains approximately constant (50%) at $L_{\text{IR}} > 10^{12}\ L_{\odot}$.

As we saw in §5, the majority of the IR power-law galaxies have SEDs similar to the

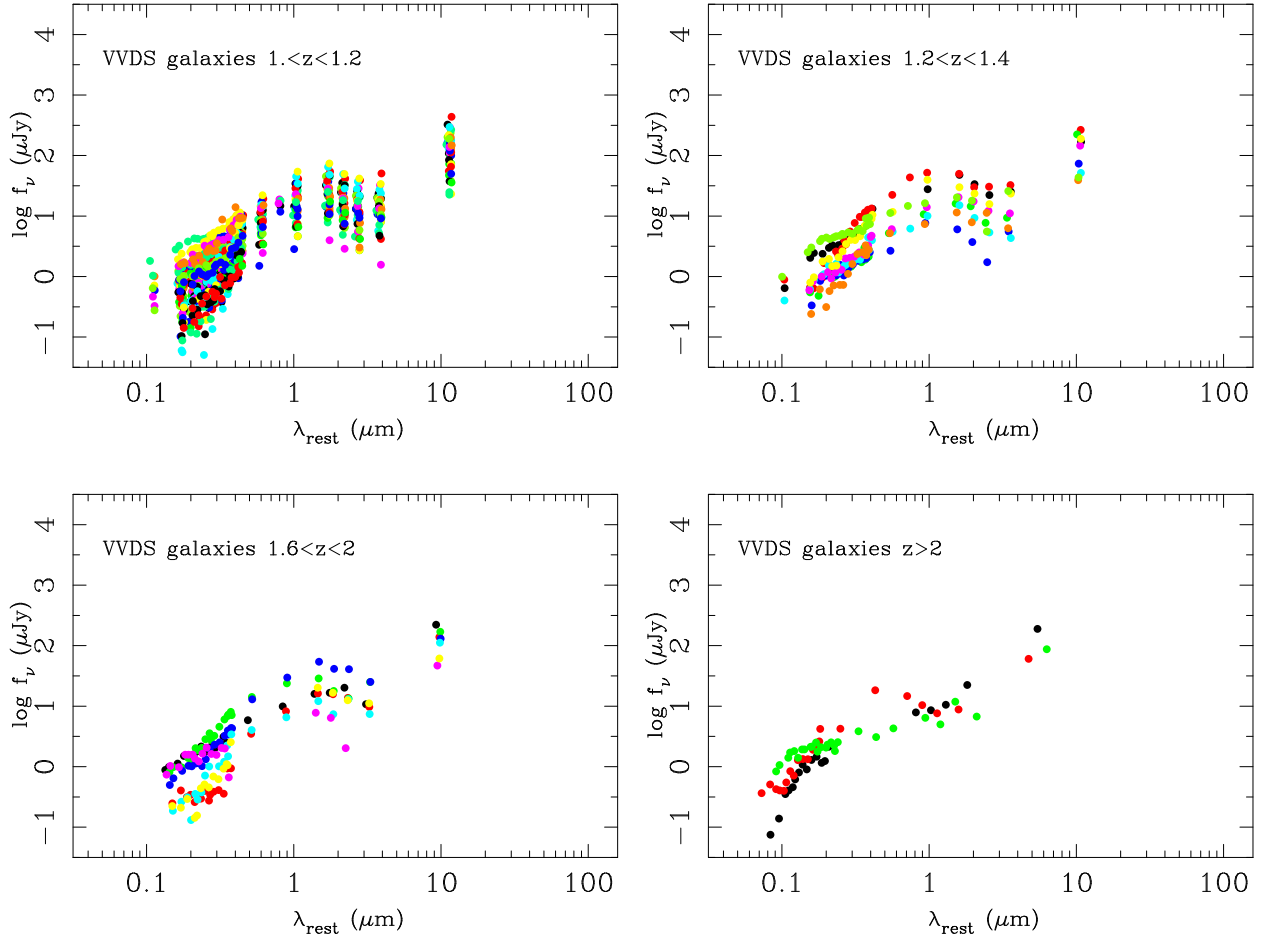


Fig. 6.— SEDs of VVDS galaxies ($I_{\text{AB}} \leq 24$) in the CDFS at $z > 1$ included in the sample of predominantly star-forming galaxies selected at $24 \mu\text{m}$ by Pérez-González et al. (2005). The galaxies are plotted in different redshift intervals. At $1 < z < 2$ the $1.6 \mu\text{m}$ stellar bump is very prominent, unlike the case of the IR power-law galaxies (see Figs. 2, 3, and 4).

average SED templates shown in Fig. 2. If we extrapolated these templates, the IR power-law galaxies would satisfy the criterion for the warm ULIRG class, so it is likely that a large fraction of the IR power-law galaxies in the ULIRG category, together with galaxies detected in X-rays, contain an AGN.

6.2. IR Power-Law galaxies Compared With High- z Star-forming Galaxies

Pérez-González et al. (2005) and LeFloc’h et al. (2005) have studied the evolution of the IR luminosity of $24\ \mu\text{m}$ -selected galaxies in the CDFS and the Hubble Deep Field North (HDFN) out to a redshifts of $z = 1$ and $z = 3$, respectively. They find that ULIRGs dominate the galaxy population at $z > 2$, and make a significant contribution ($\simeq 50\%$) in the $1 < z < 2$ redshift interval, whereas at $z < 1$ they appear to be extremely rare. They excluded galaxies with SEDs increasing monotonically from the optical to the IR, that is, galaxies similar to those in our sample, because they were interested in purely star-forming galaxies.

The IR power-law galaxies constitute a small fraction, approximately 10 – 15%, of this ULIRG population at $z > 1$. This fraction is similar to that of warm SED ULIRGs among SCUBA/VLA selected high- z sources in the Lockman Hole (Egami et al. 2004), the fraction of AGN identified by means of the shape of the SED in high- z submillimeter galaxies (Ivison et al. 2004), and the percentage of warm ULIRGs in the local Universe.

Egami et al. (2004) showed that the SEDs of their SCUBA/VLA selected high- z galaxies divided into cool and warm ULIRGs, with the former showing a significant stellar bump at $1.6\ \mu\text{m}$. To further investigate the nature of the IR power-law ULIRGs, we will compare them with high- z star-forming LIRGs and ULIRGs in Pérez-González et al. (2005). We have used all the IR ($24\ \mu\text{m}$) selected galaxies at $z > 1$ with spectroscopic redshifts from the VVDS without evidence for the presence of an AGN (i.e., galaxies without an X-ray detection and/or a QSO spectroscopic identification). Their SEDs are shown in Fig. 6 in different redshift bins.

The SEDs of star-forming galaxies selected at $24\ \mu\text{m}$ and identified by the VVDS in the $1 < z < 2$ redshift range show a very pronounced $1.6\ \mu\text{m}$ stellar bump (there are only three VVDS galaxies at $z > 2$ and we cannot assess the nature of their SEDs), unlike the IR power-law galaxies (see Figs. 2, 3, and 4). This result tends to confirm the arguments in Appendix A based on local LIRGs and ULIRGs that the power-law behavior is not characteristic of star formation, but it indicates the presence of an AGN. (We cannot exclude intense star formation in the IR power-law galaxies, or even the possibility that star formation could

dominate the bolometric luminosity of these galaxies.) One caution is that these VVDS objects are optically bright ($I_{AB} \leq 24$) and therefore are probably biased toward very massive galaxies. That is, this spectroscopic sample probes the high end of the mass function at a given redshift, revealing galaxies that contain a significant population of evolved stars which might dominate the total mass of the galaxy and make the $1.6 \mu\text{m}$ bump very prominent.

7. X-ray properties

7.1. X-ray vs optical

Bauer et al. (2004, and references therein) have demonstrated that X-ray-to-optical flux ratios can be useful for distinguishing between AGN and star-forming galaxies for sources detected in deep (1 – 2 Ms) X-ray exposures. In particular, one of the criteria these authors used to classify sources as AGN is $\log f_{0.5-8\text{keV}}/f_R > -1$, whereas star-forming and normal galaxies have $\log f_{0.5-8\text{keV}}/f_R < -1$. We have used this approach to probe the nature of the IR power-law galaxies. Fig. 7 compares the COMBO-17 R -band magnitudes and the observed 0.5 – 8 keV fluxes for the galaxies in our sample. We also show the regions occupied by AGN and star-forming galaxies, adapted from Bauer et al. (2004). All but one of the IR power-law galaxies detected in X-rays are located in the area occupied by AGN ($\log f_{0.5-8\text{keV}}/f_R > -1$), and their place in the diagram is consistent with these galaxies having X-ray luminosities $L_{0.5-8\text{keV}} > 10^{42.5} \text{ erg s}^{-1}$ (see Bauer et al. 2004, and below). None of the IR power-law galaxies detected in X-rays would be classified as a star-forming galaxy based on its X-ray luminosity (i.e., $L_{0.5-8\text{keV}} < 10^{42} \text{ erg s}^{-1}$).

Most of the IR power-law galaxies not detected in X-rays tend to occupy a similar region as the X-ray detected galaxies (but as X-ray upper limits) in the R -band vs. 0.5 – 8 keV diagram. According to Bauer et al. (2004) the location of these galaxies in Fig. 7 is consistent with them having upper limits to their X-ray luminosities above $L_{0.5-8\text{keV}} \simeq 10^{41.5} \text{ erg s}^{-1}$ (see below). By this test, they are either very obscured in the X-rays or they could be dominated by star-formation. The lack of a $1.6 \mu\text{m}$ evolved stellar bump argues for the former explanation.

For X-ray sources in the CDFS, Szokoly et al. (2004) find that most X-ray type 2 QSOs (that is, galaxies absorbed in X-rays) have $R > 24 \text{ mag}$, whereas type 1 QSOs tend to be optically bright (see also our Fig. 7 since there is a good correspondence between BLAGN and X-ray type 1 QSOs). If the IR power-law galaxies not detected in X-rays in our sample contain an AGN, their optical magnitudes make them candidates to be X-ray type 2 (absorbed) AGN, also consistent with the fact that they show SEDs similar to the NLAGN

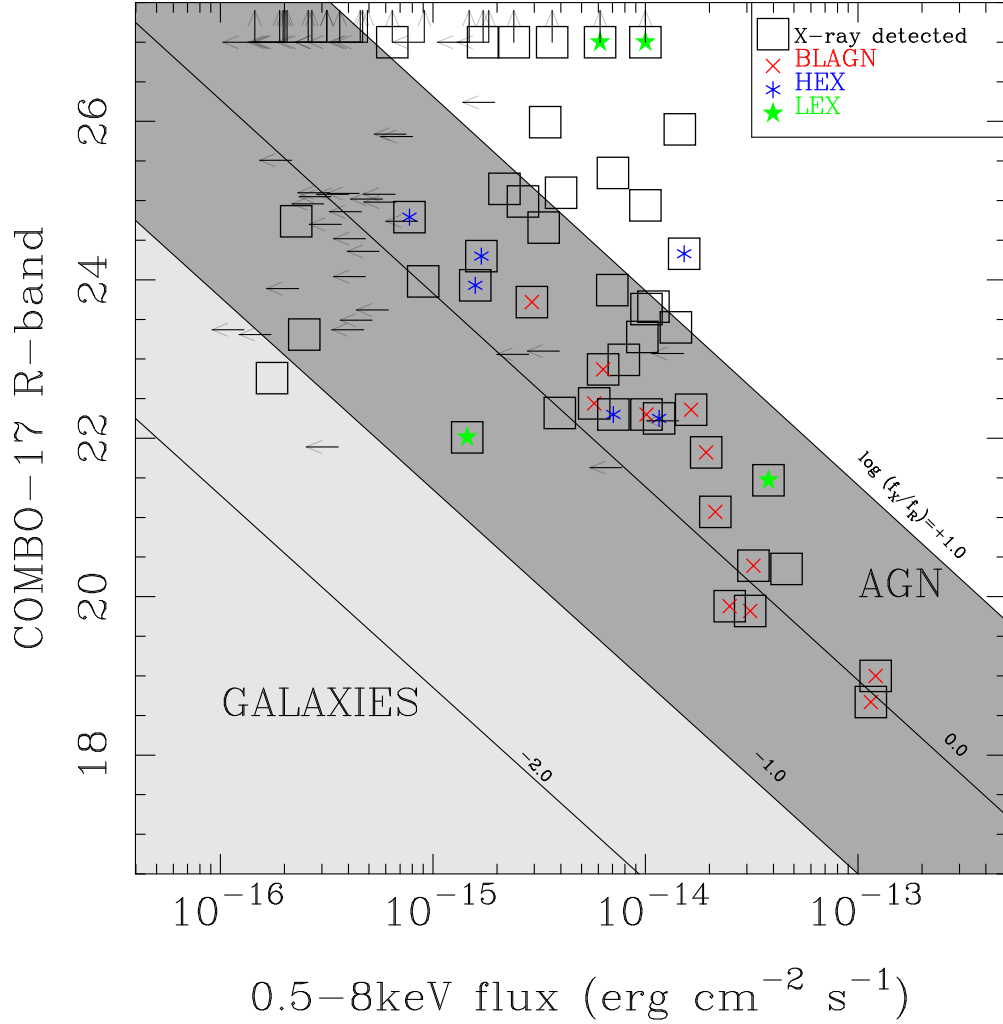


Fig. 7.— COMBO-17 R -band magnitudes (Wolf et al. 2004) vs. the *Chandra* full-band X-ray fluxes for X-ray detections and non-detections in the IR power-law sample. When available, we show the optical spectroscopic classification from Szokoly et al. (2004). Those galaxies in our sample not detected by COMBO-17 are displayed at an upper limit of $R = 27$ mag. The lightly shaded area is the approximate location of “normal” (star-forming) galaxies, and the dark shaded area is the location of AGN, adapted from Bauer et al. (2004).

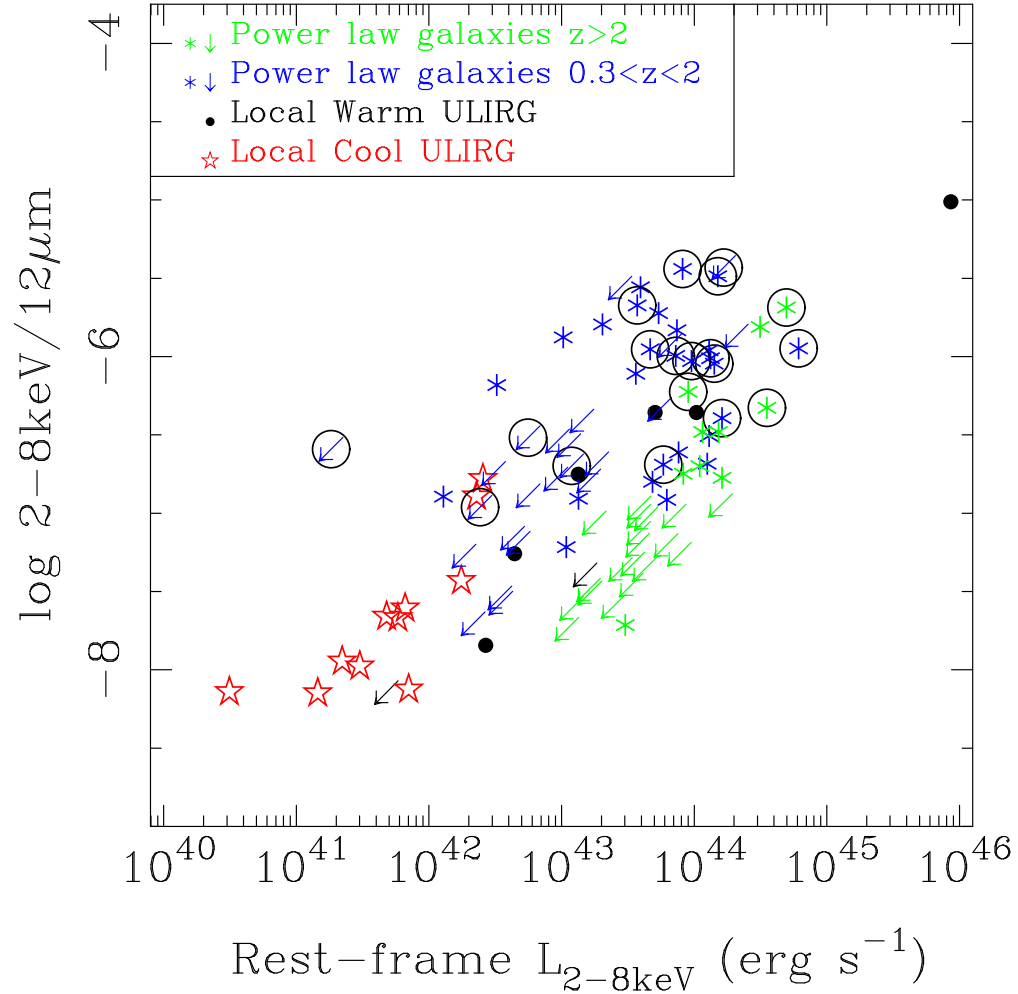


Fig. 8.— Rest-frame 2 – 8 keV luminosity vs. the rest-frame hard X-ray to $12\mu\text{m}$ flux ratio for the IR power-law SED galaxies (asterisks) compared with local examples of warm (AGN dominated, filled dots) and cool ULIRGs (with and without AGN in their nuclei, open star symbols). For the warm ULIRG sample we use all the galaxies in the original sample of Sanders et al. (1988) with detections in all four IRAS bands. We note that a few of those galaxies are not strictly ULIRGs, that is, they have $L_{\text{IR}} < 10^{12} L_{\odot}$, but they have been optically identified as AGN. The X-ray data for the local Universe ULIRGs are from Reeves & Turner (2000), Boller et al. (2002), Ptak et al. (2003), Franceschini et al. (2003), and Risaliti et al. (2000, and references therein). The IR power-law galaxies have been divided into two redshift intervals. The open circles denote those IR power-law galaxies in the BLAGN SED category.

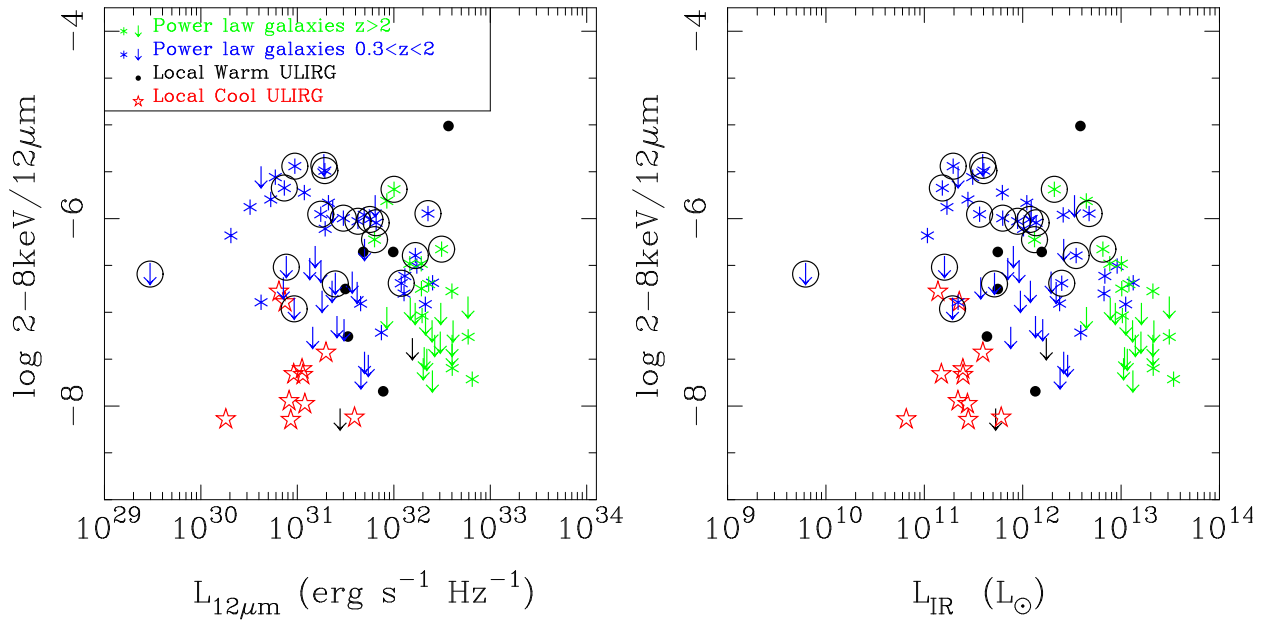


Fig. 9.— Rest-frame $12\mu\text{m}$ luminosity (left panel) and total IR $8 - 1000\mu\text{m}$ luminosity (right panel), both computed as described in §6.1, vs. the rest-frame hard X-ray to mid-IR flux ratio for the power-law SED galaxies (asterisks) compared with local examples of warm (AGN dominated, filled dots) and cool ULIRGs (open star symbols). The open circles denote those IR power-law galaxies in the BLAGN-SED category.

and ULIRG categories.

7.2. X-ray vs. IR

As shown in §6, a large fraction of the galaxies in our sample are ULIRGs. Local Universe ULIRGs are known to be intrinsically faint hard X-ray emitters — typically $L_{2-10\text{keV}} = 10^{41} - 10^{43} \text{ erg s}^{-1}$ (see Risaliti et al. 2000; Franceschini et al. 2003; Ptak et al. 2003, and also Fig. 8). Warm ULIRGs and those containing AGN tend to have higher X-ray luminosities (Fig. 8). The origin of the hard X-ray continuum of ULIRGs is still uncertain, but for some cool ULIRGs the extended nature of their soft X-ray emission and the shape of the X-ray spectra seem to indicate that the X-rays are produced by star formation (Franceschini et al. 2003, Ptak et al. 2003). Risaliti et al. (2000) found that there is a significant fraction of LIRGs and ULIRGs optically classified as AGN that do not show any evidence of X-ray activity even in the *BeppoSAX* 20 – 200 keV band, suggesting that these sources are completely Compton thick ($N_{\text{H}} > 10^{25} \text{ cm}^{-2}$).

To further understand the nature of the IR power-law galaxies in the CDFS, their X-ray and IR properties are compared with their local Universe analogs in Figs. 8 and 9. For the IR power-law galaxies we calculate the rest-frame 2 – 8 keV X-ray luminosities (not corrected for absorption) assuming an intrinsic photon index of $\Gamma = 1.8$ for which the k-corrections at low redshift ($z < 2$) are relatively small (Barger et al. 2005), and using equation 1 from Alexander et al. (2003b). Fig. 8 shows the rest-frame 2 – 8 keV to $12 \mu\text{m}$ flux ratio vs. the rest-frame 2 – 8 keV luminosity. Fig. 9 shows the same ratio vs. the rest-frame $12 \mu\text{m}$ and IR luminosities for the IR power-law galaxies.

The majority of the galaxies in our sample in the BLAGN SED class show hard X-ray luminosities $L_{2-8\text{keV}} \gtrsim 10^{43} - 10^{44} \text{ erg s}^{-1}$ (see Fig. 8), as demonstrated among others by Zheng et al. (2004), Szokoly et al. (2004), and Barger et al. (2005), based on spectroscopic classifications. Their hard X-ray to mid-IR ratios are similar to those of X-ray selected galaxies in the local Universe (e.g., the Piccinotti et al. 1982 sample).

The IR power-law galaxies in the NLAGN+ULIRG SED category show a broad range of hard X-ray to mid-IR ratios (also observed in general for X-ray sources with $24 \mu\text{m}$ counterparts, see Rigby et al. 2004), although in general below those of the BLAGN SED category. They show hard X-ray luminosities in the range $L_{2-8\text{keV}} = 10^{42} - 10^{44} \text{ erg s}^{-1}$. Both in terms of the hard X-ray luminosities and 2 – 8 keV/ $12 \mu\text{m}$ ratios, the NLAGN SED galaxies in our sample are similar to the local Universe warm ULIRGs. Local cool ULIRGs, on the other hand, tend to have hard X-ray luminosities (not corrected for absorption)

$L_{2-8\text{keV}} < 2 \times 10^{42} \text{ erg s}^{-1}$. We find that the IR power-law galaxies detected in X-rays with values of the photon index typical of highly absorbed or Compton thick X-ray emission ($\Gamma < 1$, Bauer et al. 2004) tend to have $\log(2-8\text{keV}/12\mu\text{m}) \lesssim -6.5$, which could explain the smaller hard X-ray to mid-IR flux ratios if the rest-frame hard X-rays are heavily absorbed.

The IR power-law galaxies not detected in X-rays tend to have upper limits to the 0.5–8 keV luminosities and the 2–8keV/12 μm ratios in the observed range of the NLAGN SED galaxies detected in X-rays. These properties are also similar to those of some of the warm ULIRGs in the local Universe.

In terms of the rest-frame 12 μm luminosities, the IR power-law galaxies in the BLAGN SED category span a larger range than in hard X-ray luminosities (Fig. 8 and 9). The high- z IR power-law galaxies in the NLAGN+ULIRG SED class tend to be amongst the most luminous objects at 12 μm and in the IR. Since there is a larger overlap in 12 μm luminosities between the BLAGN and NLAGN+ULIRG SED categories than in hard X-ray luminosities, it is likely that the smaller 2–8keV/12 μm ratios in the latter class are due to absorbed X-ray emission, as also suggested by the fitted photon indices, unless BLAGN SED galaxies are intrinsically more X-ray luminous than the NLAGN+ULIRG SED galaxies.

7.3. X-ray stacking of undetected galaxies

We stacked the X-ray data of the 17 individually undetected galaxies at off-axis angles of less than $9'$ and lying further away than 3 times the 90% encircled energy radii of other X-ray sources in the field, following the procedure of Immler et al. (2005) and Worsley et al. (2005). This yielded a significant detection in the soft band (3.9σ) and a tentative detection in the hard band (2.2σ). The corresponding average soft-band and hard-band fluxes are $\approx 6.5 \times 10^{-18} \text{ erg cm}^{-2} \text{ s}^{-1}$ and $\approx 2.7 \times 10^{-17} \text{ erg cm}^{-2} \text{ s}^{-1}$, calculated assuming $\Gamma = 1.4$; assuming a non detection in the hard band, the 3σ upper limit is $< 5.6 \times 10^{-17} \text{ erg cm}^{-2} \text{ s}^{-1}$. The average X-ray spectral slope is $\Gamma \approx 0.9$ (hard-band detected) or $\Gamma > 0.3$ (hard-band undetected). For $z = 2$ the observed soft and hard-band luminosities of the detections would be $2 \times 10^{41} \text{ erg s}^{-1}$ and $8 \times 10^{41} \text{ erg s}^{-1}$, respectively. This is consistent with obscured AGN.

8. Comparison with Predictions for Obscured Infrared AGN

Ueda et al. (2003) and Treister et al. (2004) have put forward models to reconcile the observed redshift distribution of AGN and that predicted by the 2–10 keV X-ray background

synthesis models. Ueda et al. (2003) derive a ratio of about 1:1 for hard X-ray detections of obscured ($N_{\text{H}} > 10^{22} \text{ cm}^{-2}$) to unobscured AGN. Treister et al. (2004) specifically modeled the Great Observatories Origins Deep Survey (GOODS) CDFS and HDFN fields. They also predict that a faint $24 \mu\text{m}$ -selected sample will have about a 2:1 to 3:1 ratio of obscured to unobscured AGN. In the deep *Chandra* fields the spectroscopically observed fraction of obscured to unobscured AGN is 2 to 1 at $z \simeq 0.7$ (Barger et al. 2003).

We now compare these predictions with our results on IR power-law galaxies and X-ray detected AGN. The FOV of our study is approximately 0.1 deg^2 , although the X-ray sensitivity is not uniform across the field. Of the CDFS galaxies detected in the hard X-ray band ($> 2 \times 10^{-16} \text{ erg cm}^{-2} \text{ s}^{-1}$, to ensure that they are AGN), 116 are detected at $24 \mu\text{m}$ down to approximately $80 \mu\text{Jy}$, where the $24 \mu\text{m}$ counts are $\sim 80\%$ complete. Treister et al. (2004) infer that among those CDFS AGN with spectroscopic redshifts about 55% have $N_{\text{H}} > 10^{22} \text{ cm}^{-2}$ (see also Rigby et al. 2004). Assuming that this fraction remains the same for those X-ray sources detected at $24 \mu\text{m}$, then we would expect approximately $52/0.8 = 65$ unobscured and $64/0.8 = 80$ obscured AGN among the hard X-ray sources detected at $24 \mu\text{m}$. For a FOV of 0.1 deg^2 Treister et al. (2004) models would predict ~ 88 unobscured sources (type 1) and $\sim 180 - 250$ obscured AGN with $f_{24\mu\text{m}} \gtrsim 80 \mu\text{Jy}$. The smaller number of observed unobscured sources is probably due to the fact that we are using the entire X-ray FOV, whereas the Treister et al. (2004) predictions for the GOODS field are for the area with the most sensitive X-ray observations (see below).

How many of these obscured galaxies can be accounted for? In our sample of IR power-law galaxies, we have $54/0.8 = 68$ galaxies not detected in hard X-rays (see Table 2). As we showed in §6 most of these galaxies have IR luminosities above $2 \times 10^{12} L_{\odot}$. Moreover, the IR power law galaxies not detected in X-rays have upper limits to the rest-frame $2 - 8 \text{ keV} / 12 \mu\text{m}$ flux ratios that are typical of absorbed AGN. Adding the power-law IR galaxies not detected in hard X-rays and the predicted number of obscured hard X-ray sources detected at $24 \mu\text{m}$, we would have approximately 148 obscured AGN, and thus a ratio of obscured to unobscured $24 \mu\text{m}$ detected AGN of 2:1.

If we restrict ourselves to the most sensitive X-ray area (off-axis angles $\leq 8'$, area $\simeq 0.05 \text{ deg}^2$), following the same reasoning as above, we find 90 obscured AGN and 47 unobscured AGN at $24 \mu\text{m}$. Treister et al. (2004) predict an AGN number count at $24 \mu\text{m}$ of approximately 100–130 for a field this size, consistent with our data. The observed obscured to unobscured ratio of $24 \mu\text{m}$ detected AGN remains 2:1 for the most sensitive X-ray area.

Thus, although our results are consistent with the lower obscured to unobscured ratio of Treister et al. (2004), we have not identified all of the predicted fraction of obscured AGN. However, it is likely that the *Spitzer* data will eventually reveal a significant number

of additional obscured AGN. In the 1 Jy sample of ULIRGs, Veilleux et al. (1999) find that approximately 30% of galaxies are optically classified as Seyfert. If the fraction in the local Universe is similar to that at higher redshifts, it is possible that we are still missing some 50 ULIRGs (with no X-ray detections) from our sample of IR power-law galaxies containing an AGN at $z > 1$. Specifically, many galaxies may be analogous to the cool ULIRGs in the local Universe that host an AGN but have SEDs not dominated by the AGN emission (e.g., Mrk 273, UGC 5101), and are not bright in X-rays (see §7.2). A significant number of additional obscured AGN can be identified by comparing radio and IR measurements. For example, Donley et al. (2005) find 16 radio-bright AGN in the HDFN that are above our threshold for $24\mu\text{m}$ detection but below the threshold for the X-ray catalogs of the region.

9. Conclusion

The presence of power-law emission in the optical and/or IR is usually taken to indicate an AGN. In this paper, we investigated the nature of the IR power-law galaxies in the CDFS. We emphasized probing whether those not detected in X-rays are part of a population of obscured AGN.

We used *Spitzer*/MIPS $24\mu\text{m}$ observations ($f_{24\mu\text{m}} \gtrsim 80 \mu\text{Jy}$) in the CDFS to select a sample of 92 galaxies showing power-law-like emission in the IRAC bands ($f_\nu \propto \nu^\alpha$, with $\alpha < -0.5$). Approximately 53% (49 galaxies) of these IR power-law galaxies are detected in at least one of the *Chandra* X-ray bands, and they comprise approximately 30% of the hard X-ray sources with $24\mu\text{m}$ counterparts in the CDFS. For those IR power-law galaxies not detected in X-rays we have derived upper limits to the *Chandra* X-ray band fluxes that are consistent with their harboring AGN.

The main properties of our sample of IR power-law galaxies are as follows:

- *Spectroscopic and photometric redshifts.* The redshifts of the IR power-law galaxies are between 0.6 and 3, although most of the galaxies in the sample lie at $z > 1$, in contrast with the observed spectroscopic grouping at $z \simeq 0.7$ for X-ray sources and galaxies with $I_{\text{AB}} \leq 24$ in the CDFS.
- *Shape of the SED.* The IR power-law galaxies detected in X-rays are almost equally divided between BLAGN (40%) and NLAGN+ULIRG (60%) classes, whereas the majority of the galaxies not detected in X-rays have SEDs in the NLAGN+ULIRG class as they tend to be optically fainter, and possibly more obscured. The steepest IRAC SEDs correspond to $\nu^{-2.8}$, which is also a limit found for optically-faint X-ray AGN

and for a complete sample of flat spectrum radio sources. This slope evidently defines limiting behavior for the optical-IR SEDs of AGN.

- *IR Luminosities.* Approximately 40% of the sample of IR power-law galaxies are ULIRGs, and a further 30% are in the hyperluminous IR galaxy class. At the lower IR luminosity end ($L_{\text{IR}} = 10^{11} - 10^{12} L_{\odot}$) the majority of galaxies are detected in X-rays, particularly for those in the BLAGN SED category. At the upper end of the IR luminosity distribution the fraction of X-ray detected galaxies is approximately 50% of the sample of IR power law galaxies, although the majority of the IR power-law galaxies not detected in X-rays have IR luminosities above $10^{12} L_{\odot}$.
- *IR power-law galaxies vs. IR selected star-forming galaxies at high z .* The ULIRGs in the IR power-law galaxy sample represent a small fraction, 10 – 15%, of the high- z ULIRG population of predominantly star-forming galaxies detected with *Spitzer* (Pérez-González et al. 2005). The SEDs of IR ($24 \mu\text{m}$ selected) star-forming galaxies identified by the VVDS ($I_{\text{AB}} \leq 24$) in the $1 < z_{\text{sp}} < 2$ redshift interval are dominated by stellar emission unlike the majority of the IR power-law galaxies.
- *X-ray Properties of X-ray detected IR power-law galaxies.* All the X-ray detected galaxies in our sample have rest-frame 2 – 8 keV luminosities above $10^{42} \text{ erg s}^{-1}$. Galaxies in the BLAGN SED category have rest-frame hard X-ray luminosities $L_{2-8\text{keV}} \gtrsim 10^{43} - 10^{44} \text{ erg s}^{-1}$, and their X-ray to mid-IR flux ratios are similar to those of local X-ray selected galaxies. X-ray galaxies in the NLAGN+ULIRG SED class show in general lower X-ray luminosities ($L_{2-8\text{keV}} = 10^{42} - 10^{44} \text{ erg s}^{-1}$) and X-ray to mid-IR ratios lower than those of the BLAGN SED galaxies, as well as X-ray photon indices indicative of absorbed X-ray emission.
- *X-ray Properties of IR power-law galaxies not detected in X-rays.* For these objects, the upper limits to the rest-frame 2 – 8 keV luminosities ($L_{2-8\text{keV}} < 10^{42} - 10^{44} \text{ erg s}^{-1}$) and to the hard X-ray to mid-IR flux ratios are similar to those of the X-ray detected galaxies in the NLAGN+ULIRG SED class, and consistent with those of some of the local Universe warm ULIRGs known to contain an AGN.

The upper limits to the X-ray luminosities and hard X-ray to mid-IR flux ratios, as well as the shape of the SEDs, the optical magnitudes, and the IR luminosities of the IR power-law galaxies not detected in X-rays make them good candidates to contain IR-bright X-ray-absorbed AGN. Adding together the IR power-law galaxies not detected in hard X-rays and the fraction of absorbed ($N_{\text{H}} > 10^{22} \text{ cm}^{-2}$) X-ray galaxies detected at $24 \mu\text{m}$ estimated by Treister et al. (2004), we find a ratio of obscured to unobscured AGN detected at $24 \mu\text{m}$ of

about 2:1. This ratio is consistent with the (lower range of the) model predictions of Treister et al. (2004). A significant number of additional obscured AGN may eventually be revealed by *Spitzer* observations of X-ray quiet radio galaxies (Donley et al. 2005) and by further characterization of ULIRGs harboring AGN but with cool IR SEDs probably dominated by emission due to young stars.

We are grateful to the referee for comments that helped improve the paper. We thank Belinda Wilkes and Joanna Kuraszkiewicz for interesting discussions. AAH acknowledges support from the Spanish Programa Nacional de Astronomía y Astrofísica under grant AYA2002-01055. This work is based [in part] on observations made with the Spitzer Space Telescope, which is operated by the Jet Propulsion Laboratory, Caltech under NASA contract 1407. Support for this work was provided by NASA through Contract no. 960785 and 1256790 issued by JPL/Caltech. This research has made use of the NASA/IPAC Extragalactic Database (NED) which is operated by the Jet Propulsion Laboratory, California Institute of Technology, under contract with the National Aeronautics and Space Administration.

Selection of the Sample of IR Power-Law Galaxies

A.1 Optical and Near-Infrared Imaging and Band Merging

The *Spitzer* images have been supplemented with optical and near-IR datasets available from the literature: 1.) optical images (UU_pBVRI) from the ESO Imaging Survey (EIS, Arnouts et al. 2002); 2.) optical fluxes from the COMBO-17 survey (Wolf et al. 2004); 3.) RIz imaging obtained by Las Campanas Infrared Survey (Marzke et al. 1999); 4.) the *HST*/ACS $BViz$ and ground-based JHK observations from the GOODS team (Giavalisco et al. 2004); 5.) the near-IR JK data released by the EIS Deep Infrared Survey (Vandame et al. 2001); and 6.) the I -band photometry and spectroscopic redshifts published by the VVDS (Le Fèvre et al. 2004).

For the imaging data, the source detection and photometry were carried out with SEXTRACTOR. Merged catalogs with a $2''$ search radius in all the available bands were built by matching the coordinates of the $24\mu\text{m}$ sources to the deepest reference optical band, in our case the B -band. The fraction of multiple counterparts within the $2''$ search radius was less than 3 – 5% for the ground-based data and less than 15% for the *HST* data. The depth of the observations and the procedure for obtaining photometry are described in full detail by Pérez-González et al. (2005). The procedure allowed us to obtain integrated fluxes for each filter in matched apertures, and properly estimate colors for each source. For sources not detected in the reference image, we used other optical/near-IR images as the reference (if

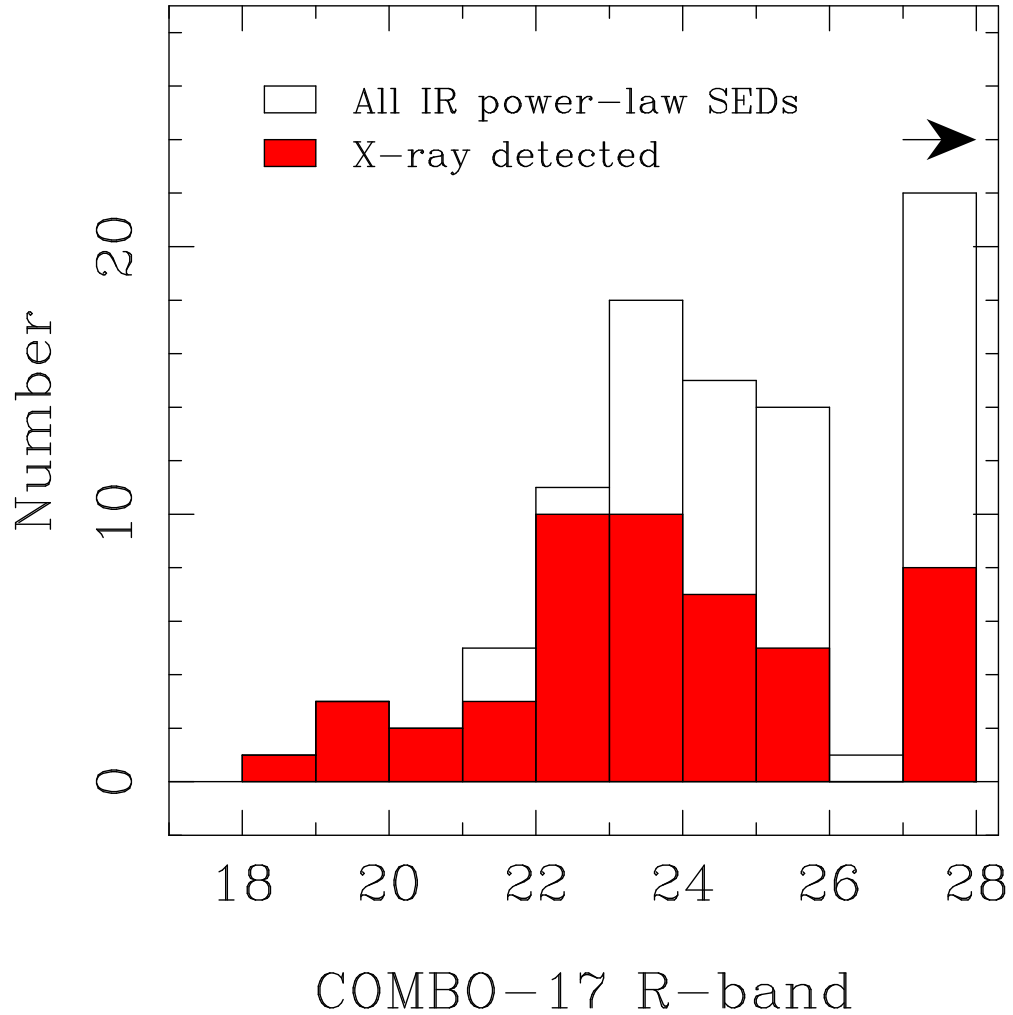


Fig. 10.— Distributions of the COMBO-17 R -band magnitudes (Wolf et al. 2004) of the 92 IR power-law SED galaxies in our sample (empty histogram). The filled histogram is galaxies detected in at least one of the *Chandra* X-ray bands. Those galaxies in our sample not detected by COMBO-17 are displayed at an upper limit of $R = 27$ mag.

possible). In the case of the IRAC and MIPS bands, the integrated flux was assumed to be that obtained from PSF fitting.

A.2 Final Sample

To obtain the final sample, the complete optical-to- $24\mu\text{m}$ SEDs were visually inspected to eliminate any possible outliers. The criteria are not uniform because of varying signal to noise from one object to another. The number of outliers was less than 15%, and were mainly galaxies with bad SEDs or galaxies resembling normal galaxies (see A.4 and Fig. 12). The final sample is composed of 92 galaxies and will be referred to as IR power-law galaxies. They have been selected without regard to X-ray properties and therefore should be unbiased in that regard. Table 1 gives *Spitzer* coordinates, flux densities and uncertainties, as well as the fitted IRAC spectral indices α for the sample of IR power-law galaxies.

Fig. 10 shows the distribution of COMBO-17 R -band magnitudes (Wolf et al. 2004) for our sample of galaxies compared to those not detected in X-rays. Galaxies not detected by COMBO-17 (22 out of 92) are shown as upper limits at $R = 27$. It is clear from this figure that the fraction of IR power-law galaxies not detected in X-rays increases towards fainter R -band magnitudes. For comparison the candidate AGN not present in the SDSS selected by Lacy et al. (2004) using IRAC colors are optically brighter than our sample, with R -band magnitudes in the range $R = 18.5 - 22.2$ mag.

We note that only AGN dominated galaxies will be identified with this method, and that the large fraction of X-ray identified AGN in cosmological surveys with optical to mid-IR SEDs dominated by stellar emission (Alonso-Herrero et al. 2004) will not be included in our sample.

A.3 Comparison with local Universe LIRGs and ULIRGs

Since our sample of IR power-law galaxies is selected at $24\mu\text{m}$, and thus is very likely to contain a large fraction of high redshift LIRGs and ULIRGs, it is of interest to simulate the expected SEDs using local Universe analogs.

Warm ULIRGs account for between 15 and 30% of galaxies with $L_{\text{IR}} > 10^{12} L_{\odot}$ in the Bright Galaxy Sample (Sanders et al. 1988). The fraction of IR luminous galaxies (LIRGs, $10^{11} L_{\odot} < L_{\text{IR}} < 10^{12} L_{\odot}$) and ULIRGs (cool and warm) containing an AGN increases with IR luminosity (Veilleux et al. 1995, 1999, Tran et al. 2001); at IR luminosities above $L_{\text{IR}} > 10^{12.3} L_{\odot}$ this fraction is over 50%. Intense star formation in dusty galaxies, on the

other hand, can also produce a bright mid-IR continuum that increases with wavelength, although the stellar bump at $1.6\ \mu\text{m}$ should still be present and prominent. As shown by Le Floch et al. (2004) and Egami et al. (2004), when present in high- z luminous IR galaxies, the $1.6\ \mu\text{m}$ rest-frame stellar bump is easily recognized using optical to mid-IR SEDs obtained virtually identically to those used here (that is, a combination of IRAC four-color photometry with data in the optical and near-IR).

To determine whether star-formation-dominated LIRGs and ULIRGs could be included in our sample, we have compiled data for local Universe LIRGs with no evidence for the presence of an AGN, as well as cool ULIRGs. Some of the galaxies in the latter category are known to host a Seyfert nucleus in their centers (e.g., Mrk 273, UGC 5101). For comparison we have also compiled data for the warm ULIRGs in Sanders et al. (1988) detected in all four IRAS bands. These warm ULIRGs are all known to contain a luminous AGN. The vast majority of the data have been taken from the NASA/IPAC Extragalactic Database (NED). We required fairly complete SEDs to include galaxies in this comparison, in particular in the near and mid-IR ranges. In addition to the data from NED, we have made use of *ISO* data for non-AGN LIRGs from Lu et al. (2003) and for cool ULIRGs from Farrah et al. (2003), as well as optical and near-IR data from Surace, Sanders, & Evans (2000). The results are shown in Fig. 11.

As expected (upper left panel of Fig. 11), local LIRGs with no AGN show a very pronounced stellar bump at $1.6\ \mu\text{m}$ whereas this bump is absent or almost absent in warm ULIRGs (upper right panel of Fig. 11). Cool ULIRGs (middle panel of Fig. 11), even those containing an AGN (i.e., UGC 5101 and Mrk 273), represent intermediate cases. Also for those galaxies with available *ISO*/PHOT-S $7.7\ \mu\text{m}$ spectroscopic data (Lutz et al. 1998; Rigopoulou et al. 1999), we can see that polycyclic aromatic hydrocarbon (PAH) emission tends to be present in those galaxies with a strong stellar continuum. Warm ULIRGs (see also SEDs in Sanders et al. 1988) show a range of spectral shapes, going from the typical shape of an optically selected QSO (IZw1) or radio loud QSO (3C273), to AGN with a more obscured UV and optical continuum (e.g., Mrk 463 and Mrk 231).

In the lower panels of Fig. 11, for a representative object of each of these classes we have redshifted the SEDs to the range of redshifts we may expect for galaxies in our sample. We also show for comparison purposes power laws in the IRAC spectral range with spectral indices $\alpha = -0.5, -0.7 - 1.0$.

Fig. 11 illustrates a number of important points. First, nearby ($z \leq 0.4 - 0.5$) IR bright galaxies could be included in our initial sample since their rest-frame $4 - 8\ \mu\text{m}$ continuum rises steeply resembling the shape of a power law. However, once the complete optical to mid-IR SEDs are constructed, this kind of galaxy is easily identified and therefore excluded

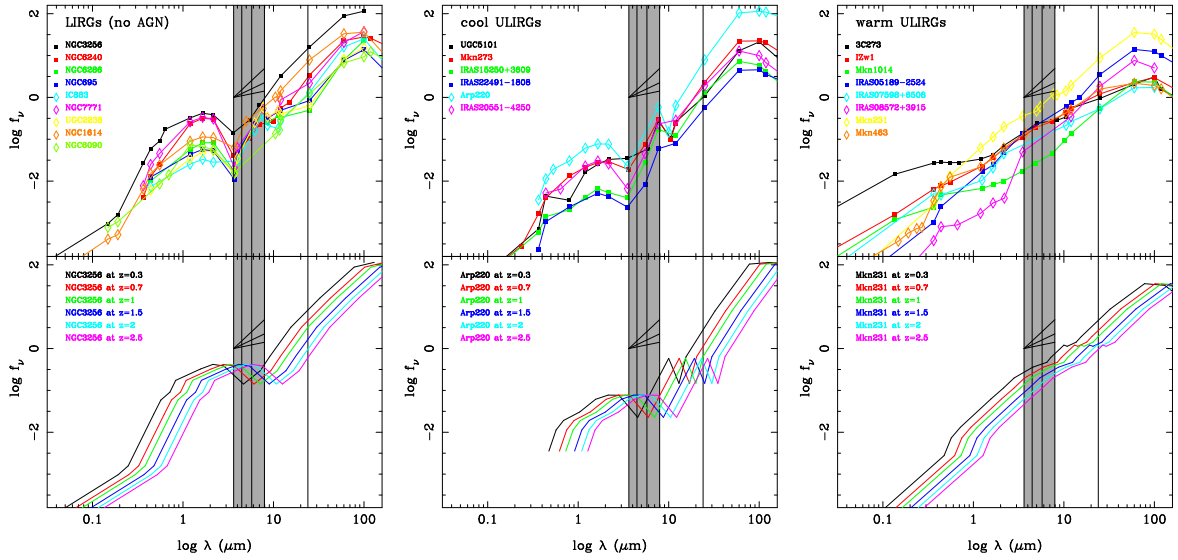


Fig. 11.— The upper panels from left to right are SEDs of local Universe LIRGs with no evidence for the presence of an AGN, cool ULIRGs, and warm ULIRGs, respectively. The lower panels show one SED of each type as it would be observed for galaxies at different redshifts. We show the spectral range covered by the IRAC bands (shaded area), and the MIPS 24 μm band. We have also plotted power laws ($f_\nu \propto \nu^\alpha$) in the IRAC spectral range with spectral indices $\alpha = -0.5, -0.7 - 1.0$.

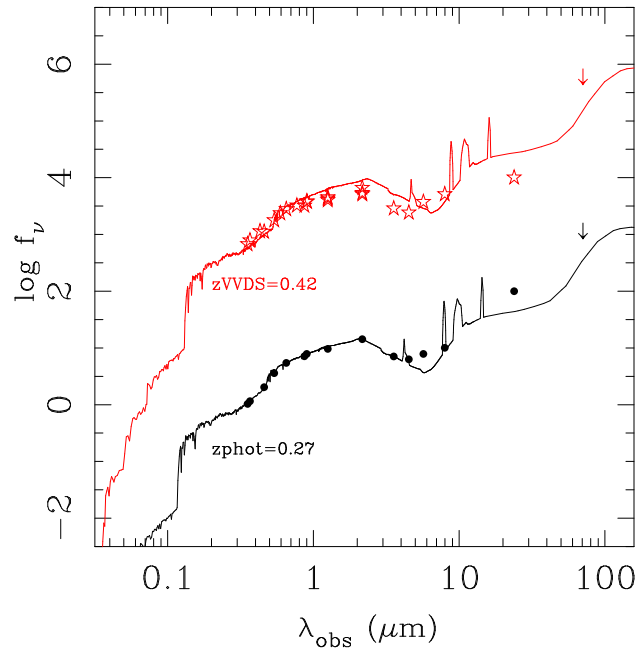


Fig. 12.— Two nearby galaxies initially selected with the IR power-law criteria that show SEDs (filled dots and stars, arbitrarily shifted for clarity) consistent with that of a normal (non-active) galaxy. The lines are a theoretical template for an Sc galaxy from Devriendt, Guiderdoni, & Sadat (1999).

from our final sample (see next section). Second, cool ULIRGs at $0.4 < z < 2$ containing a Seyfert nucleus but whose near-IR continuum is dominated by stellar emission (from either a quiescent population or a starburst), such as Mrk 273, will not be included in our final sample because the $1.6\ \mu\text{m}$ stellar bump will get redshifted into the IRAC bands. AGN whose IR SEDs are dominated by stellar emission might make up a significant fraction of the AGN identified in deep X-ray surveys (Alonso-Herrero et al. 2004; Franceschini et al. 2005), and are not selected with our criteria. Lastly, for galaxies at $z > 2$ not showing a very steep ($\alpha > -1$) IRAC continuum we may not be able to distinguish between the SED of a warm and a cool ULIRG. In such cases, we will have to use other criteria (i.e., X-ray and IR luminosities) to determine whether they are likely to contain an AGN.

A.4 Normal Galaxies

As an illustration, in Fig. 12 we show two of the galaxies eliminated from the sample whose SEDs resemble that of a normal galaxy. Both are two nearby ($z < 0.4 - 0.5$) galaxies dominated by stellar emission but showing a steeply rising rest-frame $4 - 8\ \mu\text{m}$ continuum. Although they passed screening for the initial sample, they are easily recognized as *normal galaxies from the optical to mid-IR SED, as they show the typical SED of a spiral galaxy with a prominent $1.6\ \mu\text{m}$ stellar bump.*

Normal galaxies in our sample are also obvious because they are optically bright with respect to their X-ray fluxes (or to the upper limits to the fluxes — see further discussion in §7.1). Of the two galaxies shown in Fig. 12, one has a spectroscopic redshift from the VVDS, and for the second one we use our own phot- z (see Fig. 12). We find that both galaxies have X-ray upper limits to the *Chandra* full-band luminosity of $L_{0.5-8\text{keV}} \leq 10^{41}\ \text{erg s}^{-1}$, well below the typical luminosity of a Seyfert nucleus.

REFERENCES

- Alexander, D. M. et al. 2002, ApJ, 568, L85
- Alexander, D. M. et al. 2003a, AJ, 126, 539
- Alexander, D. M., Bauer, F. E., Brandt, W. N., Hornschemeier, A. E., Vignali, C., Gamire, G. P., Schneider, D. P., Chartas, G., & Gallagher, S. C. 2003b, AJ, 125, 383
- Alexander, D. M., Smail, I., Bauer, F. E., Chapman, S. C., Blain, A. W., Brandt, W. N., & Ivison, R. J. 2005, Nature, 434, 738

- Almaini, O., Lawrence, A., & Boyle, B. J. 1999, MNRAS, 305, L59
- Alonso-Herrero, A. et al. 2004, ApJS, 154, 155
- Arnouts, S., Vandame, B., Benoist, C., Groenewegen, M. A. T., da Costa, L., Schirmer, M., Mignani, R. P. & Slijkhuis, R., 2002, VizieR On-line Data Catalog, 337, 90740
- Barger, A. J. et al. 2003, AJ, 126, 632
- Barger, A. J., Cowie, L. L., Mushotzky, R. F., Yang, Y., Wang, W.-H., Steffen, A. T., & Capak, P. et al. 2005, AJ, 129, 578
- Barmby, P. et al. 2005, in preparation
- Bauer, F. E., Alexander, D. M., Brandt, W. N., Schneider, D. P. et al. 2004, AJ, 128, 2048
- Bertin, E. & Arnouts, S. 1996, A&AS, 117, 393
- Boller, Th., Gallo, L. C., Lutz, D., & Sturm, E. 2002, MNRAS, 336, 1146
- Brandt, W. N. & Hasinger, G. 2005, ARA&A, 43, in press (astro-ph/0501058)
- Caputi et al. 2005, in preparation
- Carleton, N. P. et al. 1987, ApJ, 318, 595
- Comastri, A. et al. 1995, A&A, 296, 1
- Devriendt, J. E. G., Guiderdoni, B., & Sadat, R. 1999, A&A, 350, 381
- Dole, H. et al. 2004, ApJS, 154, 87
- Donley, J. L., Rieke, G. H., Rigby, J. R., & Pérez-González, P. G. 2005, ApJ, in press (astro-ph/0507676)
- Edelson, R. A., Malkan, M. A., & Rieke, G. H. 1987, ApJ, 321, 233
- Egami, E. et al. 2004, ApJS, 154, 130
- Elvis, M. et al. 1994, ApJS, 95, 1
- Fabian, A., & Iwasawa, K. 1999, MNRAS, 303, L34
- Fadda, D. et al. 2002, A&A, 383, 838

- Farrah, D., Afonso, J., Efstathiou, A., Rowan-Robinson, M., Fox, M. & Clements, D. 2003, MNRAS, 343, 585
- Fazio, G. G. et al. 2004, ApJS, 154, 10
- Franceschini, A., Braito, V., Persic, M., Della Ceca, R., Bassani, L., Cappi, M., Malaguti, G., Palumbo, G. G. C., Risaliti, G., Salvati, M., & Severgnini, P. 2003, MNRAS, 343, 1181
- Franceschini, A. et al. 2005, AJ, 129, 2074
- Giacconi, R. et al. 2002, ApJS, 139, 369
- Giavalisco, M. et al. 2004, ApJ, 600, L93
- Gordon, K. D. et al. 2005, PASP, 117, 503
- Huang, J.-S. et al. 2004, ApJS, 154, 44
- Immler, S. et al. 2005, in preparation
- Ivezić, Z. et al. 2002, AJ, 124, 2364
- Iverson, R. J. et al. 2004, ApJS, 154, 124
- Klaas, U. et al. 2001, A&A, 379, 823
- Kleinmann, S. G., Hamilton, D., Keel, W. C., Wynn-Williams, C. G., Eales, S. A., Becklin E. E., & Kuntz K. D., 1988, ApJ, 316, 161
- Kuraszkiewicz, J. K. et al. 2003, ApJ, 590, 128
- Lacy, M. et al. 2004, ApJS, 154, 166
- Lacy, M. et al. 2005, MmSAI, 76, 154
- Le Fèvre, O. et al. 2004, A&A, 428, 1043
- Le Floch, E. et al. 2004, ApJS, 154, 170
- Le Floch, E. et al. 2005, ApJ, in press (astro-ph/0506462)
- Lu, N. et al. 2003, ApJ, 588, 199
- Lutz, D., Spoon, H. W. W., Rigopoulou, D., Moorwood, A. F. M., & Genzel, R. 1998, ApJ, 505, L103

- Marzke, R. et al. 1999, in ASP Conf. Ser. 191: Photometric Redshifts and the Detection of High Redshift Galaxies, p. 148
- Neugebauer, G. et al. 1979, ApJ, 230, 79
- Papovich, C. et al. 2004, ApJS, 154, 70
- Pérez-González, P. G. et al. 2005, ApJ, 630, 82
- Piccinotti, G. et al. 1982, ApJ, 253, 485
- Ptak, A., Heckman, T., Levenson, N. A., Weaver, K., & Strickland, D. 2003, ApJ, 592, 782
- Ranalli, P., Comastri, A., & Setti, G. 2003, A&A, 399, 39
- Reeves, J. N. & Turner, M. J. L. 2000, MNRAS, 316, 234
- Rieke, G. H., & Lebofsky, M. J. 1981, ApJ, 250, 87
- Rieke, G. H. et al. 2004, ApJS, 154, 25
- Rigby, J. R. et al. 2004, ApJS, 154, 160
- Rigby, J. R., Rieke, G. H., Pérez-González, P. G., Donley, J. L., Alonso-Herrero, A., Huang, J.-S., Barmby, P., & Fazio, G. G. 2005a, ApJ, 627, 134
- Rigby, J. R., Rieke, G. H., Donley, J. L., Alonso-Herrero, A., Pérez-González, P. G., & Willner, S. P. 2005b, ApJ, submitted
- Rigopoulou, D., Spoon, H. W. W., Genzel, R., Lutz, D., Moorwood, A. F. M., & Tran, Q. D. 1999, AJ, 118, 2625
- Risaliti, G., Gilli, R., Maiolino, R., & Salvati, M. 2000, A&A, 357, 13
- Rowan-Robinson, M. 2000, MNRAS, 316, 885
- Rush, B., Malkan, M. A., & Spinoglio, L. 1993, ApJS, 89, 1
- Sanders, D. B., Soifer, B. T., Elias, J. H., Neugebauer, G., & Matthews, K. 1988, ApJ, 328, L35
- Sanders, D. B. & Mirabel, I. F. 1996, ARA&A, 34, 749
- Sanders, D. B. 2004, Advances in Space Research, 34, 535
- Silva, L., Maiolino, R., & Granato, G. L. 2004, MNRAS, 355, 973

- Spinoglio, L., Malkan, M. A., Rush, B., Carrasco, L., & Recillas-Cruz, E. 1995, *ApJ*, 453, 616
- Stern, D. et al. 2005, *ApJ*, 631, 163
- Stetson, P. B. 1987, *PASP*, 99, 101
- Stetson, P. B. 1994, *PASP*, 106, 25
- Stickel, M., Rieke, G. H., Kuehr, H., & Rieke, M. J. 1996, *ApJ*, 468, 556
- Surace, J., Sanders, D. B., & Evans, A. S. 2000, *ApJ*, 529, 170
- Szokoly, G. P. et al. 2004, *ApJS*, 155, 271
- Takeuchi, T. T., Buat, V., Iglesias-Páramo, J. Boselli, A., & Burgarella, D. 2005, *A&A*, 432, 423
- Tran, Q. D. et al. 2001, *ApJ*, 552, 527
- Treister, E. et al. 2004, *ApJ*, 616, 123
- Ueda, Y., Akiyama, M., Ohta, K., & Miyaji, T. 2003, *ApJ*, 598, 886
- Vadame, B. et al. 2001, *ArXiv Astrophysics e-prints*
- Veilleux, S., Kim, D.-C., Sanders, D. B., Mazzarella, J. M., & Soifer, B. T. 1995, *ApJS*, 98, 171
- Veilleux, S., Kim, D.-C., & Sanders, D. B. 1999, *ApJ*, 522, 113
- Ward, M. et al. 1987, *ApJ*, 315, 74
- Wilkes, B., Kuraszkiwicz, J. et al. 2005, in preparation
- Wolf, C. et al. 2004, *A&A*, 421, 913
- Worsley, M. A. et al. 2005, *MNRAS*, 357, 1281
- Yan, L., Chary, R., Armus, L., Teplitz, H., Helou, G., Frayer, D., Fadda, D., Surace, J., & Choi, P. 2005, *ApJ*, 628, 604
- Zheng, W. et al. 2004, *ApJS*, 155, 73

Table 1: *Spitzer* coordinates and flux densities, and fitted IRAC spectral indices of the IR power-law galaxy sample.

Name	RA	Dec	24 μm		3.6 μm		4.5 μm		5.8 μm		8.0 μm		70 μm		α	$\Delta\alpha$
			f_ν	Δf_ν	f_ν	Δf_ν	f_ν	Δf_ν	f_ν	Δf_ν	f_ν	Δf_ν	f_ν	Δf_ν		
(1)	(2)	(3)	μJy	μJy	μJy	μJy	μJy	μJy	μJy	μJy	μJy	μJy	μJy	μJy	(16)	(17)
mips000243	53.2050	-27.9180	141.0	29.9	11.2	1.1	10.1	1.1	11.5	2.2	17.0	2.5	-	-	-0.5	0.2
mips000309	53.1125	-27.6848	908.0	69.9	352.0	32.5	320.0	31.0	408.0	43.3	549.0	50.4	-	-	-0.6	0.2
mips000348	53.2562	-27.6951	167.0	27.2	34.5	3.2	30.8	3.0	35.5	4.2	51.6	5.1	-	-	-0.6	0.2
mips002310	53.0577	-27.9335	131.0	25.7	5.9	0.6	7.8	0.8	14.7	2.4	27.1	3.2	-	-	-2.0	0.2
mips002707	53.2816	-27.8573	80.3	24.2	15.3	1.5	16.1	1.6	16.0	2.5	24.9	3.0	-	-	-0.6	0.2
mips002775	53.2472	-27.8164	781.0	52.9	43.4	4.1	52.6	5.1	68.2	7.5	137.0	12.7	9036.5	2441.0	-1.4	0.2
mips002886	53.1422	-27.9445	108.0	27.0	8.5	0.8	11.1	1.2	14.6	2.4	21.9	2.8	-	-	-1.2	0.2
mips003108	53.1744	-27.8673	108.0	26.2	14.5	1.4	11.6	1.2	13.5	2.3	20.7	2.7	7345.1	2168.0	-0.5	0.2
mips003133	53.1953	-27.8559	145.0	25.9	12.6	1.2	13.4	1.4	18.3	2.7	19.9	2.7	6039.5	2476.2	-0.6	0.2
mips003149	53.0606	-27.8826	223.0	28.2	11.6	1.1	12.9	1.3	18.4	2.7	23.2	2.9	3427.7	1968.8	-0.9	0.2
mips003175	53.0316	-27.8705	264.0	35.2	18.0	1.7	20.0	2.0	27.2	3.4	40.2	4.2	-	-	-1.0	0.2
mips003412	52.9687	-27.8385	87.1	27.6	14.8	1.4	13.8	1.4	14.9	2.4	28.2	3.2	3228.5	1692.1	-0.8	0.2
mips003445	52.9773	-27.8516	131.0	28.9	13.1	1.3	13.8	1.4	19.5	2.8	25.6	3.0	-	-	-0.9	0.2
mips003467	52.9601	-27.8701	499.0	34.0	27.1	2.5	33.3	3.3	55.8	6.2	99.6	9.4	-	-	-1.7	0.2
mips003485	53.1053	-27.8750	136.0	23.2	9.3	0.9	12.5	1.3	20.3	2.9	26.6	3.1	3176.9	1976.9	-1.4	0.2
mips003528	53.1436	-27.8348	178.0	29.3	8.5	0.8	9.3	1.0	14.7	2.4	16.8	2.5	4655.9	1940.8	-0.9	0.2
mips003554	53.0161	-27.8915	76.4	26.3	14.4	1.4	14.7	1.5	15.0	2.5	23.2	2.9	-	-	-0.6	0.2
mips003559	53.0025	-27.8982	149.0	34.4	8.2	0.8	10.1	1.1	18.4	2.7	34.4	3.7	-	-	-1.9	0.2
mips003618	53.1489	-27.8212	519.0	41.0	14.9	1.4	16.4	1.6	30.3	3.7	36.8	3.9	3318.9	1827.6	-1.2	0.2
mips003636	52.9666	-27.8909	298.0	50.7	6.4	0.7	9.6	1.0	18.1	2.7	34.7	3.7	-	-	-2.1	0.2
mips003674	52.9928	-27.8451	833.0	50.7	23.7	2.2	25.1	2.5	42.2	4.9	86.5	8.2	8871.6	1782.9	-1.7	0.2
mips003735	53.2866	-27.7151	164.0	33.0	26.1	2.4	25.9	2.6	31.1	3.8	41.9	4.3	-	-	-0.6	0.2
mips003777	52.9372	-27.8605	219.0	33.4	13.1	1.3	14.3	1.4	18.7	2.7	17.9	2.5	-	-	-0.5	0.2
mips003888	53.1151	-27.6959	351.0	36.4	46.0	4.3	39.7	3.9	55.7	6.2	74.9	7.2	-	-	-0.7	0.2
mips003915	53.1589	-27.6625	559.0	50.6	76.0	7.1	72.5	7.1	91.6	9.9	137.0	12.7	4217.0	2434.7	-0.8	0.2
mips003938	53.1310	-27.7732	328.0	37.2	23.8	2.2	24.5	2.4	42.6	4.9	59.7	5.8	6792.0	2147.3	-1.2	0.2
mips004254	52.9558	-27.7763	91.1	22.6	14.8	1.4	15.2	1.5	20.1	2.8	35.8	3.8	4786.3	2350.8	-1.1	0.2
mips004258	53.0455	-27.7375	286.0	33.9	35.6	3.3	45.9	4.5	56.6	6.3	75.0	7.2	3104.6	2163.5	-0.9	0.2
mips004281	53.0334	-27.7110	511.0	45.1	23.9	2.2	21.7	2.2	34.5	4.1	54.8	5.4	-	-	-1.1	0.2
mips005415	53.0167	-27.6238	85.5	27.0	17.5	1.7	16.0	1.6	22.6	3.0	28.0	3.2	-	-	-0.7	0.2
mips009708	53.1802	-27.8206	144.0	24.6	18.1	1.7	19.1	1.9	29.0	3.6	28.0	3.2	-	-	-0.6	0.2
mips009714	52.9470	-27.8871	214.0	30.6	17.6	1.7	23.5	2.3	39.7	4.6	67.4	6.5	-	-	-1.7	0.2
mips009757	53.1929	-27.7755	89.9	23.5	6.8	0.7	6.3	0.7	11.0	2.2	14.6	2.3	3872.6	2061.0	-1.0	0.2
mips010697	53.1573	-27.8701	1010.0	62.1	47.1	4.4	66.3	6.5	101.0	10.9	217.0	20.0	-	-	-1.9	0.2
mips010760	53.0821	-27.7673	275.0	37.1	10.9	1.1	13.4	1.4	20.5	2.9	18.2	2.5	4497.8	1689.6	-0.8	0.2
mips010785	53.1071	-27.7183	480.0	45.3	14.1	1.4	21.8	2.2	53.8	6.0	125.0	11.6	-	-	-2.8	0.2
mips010787	53.1049	-27.7053	499.0	40.0	52.0	4.8	61.4	6.0	69.0	7.6	94.7	8.9	-	-	-0.7	0.2
mips010823	53.1110	-27.6702	116.0	29.5	13.4	1.3	14.7	1.5	15.7	2.5	32.7	3.6	-	-	-1.1	0.2
mips012254	53.2494	-27.7967	101.0	29.9	16.9	1.6	17.3	1.7	23.7	3.1	39.7	4.1	-	-	-1.1	0.2
mips012297	53.1995	-27.7092	995.0	51.3	140.0	13.0	130.0	12.6	155.0	16.6	220.0	20.3	-	-	-0.6	0.2
mips012310	53.0222	-27.7792	182.0	55.2	12.0	1.2	12.0	1.2	12.3	2.3	23.0	2.9	8669.6	2219.6	-0.8	0.2
mips012314	52.9680	-27.7981	369.0	65.2	18.3	1.7	19.9	2.0	33.0	4.0	40.9	4.2	6823.4	1936.8	-1.1	0.2
mips012329	53.2050	-27.6808	2100.0	83.4	112.0	10.3	173.0	16.8	293.0	31.1	489.0	44.9	10447.2	2050.5	-1.9	0.2
mips012371	53.0676	-27.6585	1350.0	74.5	140.0	13.0	170.0	16.5	241.0	25.6	390.0	35.8	-	-	-1.3	0.2
mips012940	53.2571	-27.9719	655.0	50.5	67.4	6.3	72.5	7.1	109.0	11.7	188.0	17.4	3184.2	2188.5	-1.3	0.2
mips013087	53.1104	-27.6766	2060.0	94.5	168.0	15.5	176.0	17.1	256.0	27.2	449.0	41.3	5296.6	2170.8	-1.3	0.2
mips013611	53.0361	-27.7930	3320.0	110.0	410.0	37.8	406.0	39.5	564.0	59.7	734.0	67.2	-	-	-0.8	0.2
mips014534	53.0061	-27.6940	234.0	51.0	24.7	2.3	26.6	2.6	31.7	3.9	50.1	5.0	-	-	-0.9	0.2
mips014635	53.1250	-27.7585	442.0	59.2	66.4	6.2	64.5	6.3	69.9	7.7	118.0	11.1	-	-	-0.7	0.2

Table 1: Continued.

Name	RA	Dec	24 μm		3.6 μm		4.5 μm		5.8 μm		8.0 μm		70 μm		α	$\Delta\alpha$
(1)	(2)	(3)	f_ν μJy	Δf_ν μJy	f_ν μJy	Δf_ν μJy	f_ν μJy	Δf_ν μJy	f_ν μJy	Δf_ν μJy	f_ν μJy	Δf_ν μJy	f_ν μJy	Δf_ν μJy	(16)	(17)
mips000314	53.0968	-27.6725	109.0	26.5	6.3	0.7	8.2	0.9	9.9	2.1	12.3	2.2	2500.3	1775.8	-0.9	0.3
mips002219	53.1311	-27.9810	252.0	31.6	10.4	1.0	12.7	1.3	12.9	2.3	18.8	2.6	3243.4	2333.4	-0.7	0.2
mips002556	53.1769	-27.9759	75.4	22.3	3.9	0.4	5.5	0.6	9.6	2.1	20.0	2.7	2985.4	2140.1	-2.1	0.2
mips002581	53.1458	-27.9871	174.0	33.6	11.2	1.1	11.2	1.2	11.1	2.2	22.3	2.8	3655.9	2526.6	-0.8	0.2
mips002613	53.2175	-27.9398	107.0	26.2	11.6	1.1	12.0	1.2	18.6	2.7	16.0	2.4	—	—	-0.5	0.2
mips002788	53.3056	-27.8057	172.0	30.3	6.7	0.7	7.6	0.8	10.2	2.1	10.2	2.1	3944.6	2395.0	-0.6	0.3
mips002957	53.0709	-27.9432	69.2	23.6	5.8	0.6	9.1	1.0	11.9	2.2	16.7	2.5	5847.9	1799.9	-1.3	0.2
mips003068	53.2262	-27.8589	53.0	24.5	3.0	0.4	3.1	0.4	8.1	2.0	12.7	2.2	—	—	-1.9	0.3
mips003181	53.0701	-27.8611	132.0	30.5	8.4	0.8	10.3	1.1	10.4	2.2	12.4	2.2	—	—	-0.5	0.3
mips003182	53.0384	-27.8622	352.0	31.2	34.4	3.2	34.8	3.4	41.9	4.8	55.8	5.5	—	—	-0.6	0.2
mips003271	52.8992	-27.8597	79.7	36.1	18.5	1.8	19.8	2.0	29.5	3.7	36.6	3.9	—	—	-0.9	0.2
mips003357	52.9408	-27.8085	103.0	24.1	5.5	0.6	6.0	0.7	11.8	2.2	14.6	2.3	2760.6	1738.4	-1.3	0.2
mips003363	52.9462	-27.8194	103.0	29.2	15.2	1.4	14.4	1.5	12.2	2.3	23.2	2.9	—	—	-0.5	0.2
mips003377	52.9609	-27.8162	133.0	29.9	9.8	1.0	10.4	1.1	17.7	2.6	16.7	2.4	—	—	-0.8	0.2
mips003395	52.9728	-27.8185	81.6	28.3	3.5	0.4	4.9	0.6	10.1	2.1	11.7	2.2	—	—	-1.6	0.3
mips003454	52.9504	-27.8540	210.0	28.8	12.6	1.2	13.2	1.3	14.9	2.4	18.8	2.6	—	—	-0.5	0.2
mips003480	53.0113	-27.9150	127.0	33.3	4.6	0.5	5.3	0.6	8.2	2.0	11.7	2.2	7112.1	2059.1	-1.2	0.3
mips003537	53.1698	-27.8241	214.0	31.2	10.4	1.0	11.7	1.2	18.0	2.7	15.0	2.4	—	—	-0.6	0.2
mips003556	53.0141	-27.8873	262.0	34.2	7.8	0.8	7.1	0.8	12.9	2.3	17.3	2.5	5296.6	2140.9	-1.0	0.2
mips003639	53.0058	-27.8737	236.0	27.2	13.3	1.3	14.6	1.5	17.2	2.6	26.0	3.1	—	—	-0.8	0.2
mips003641	53.0014	-27.8653	114.0	24.5	9.5	0.9	8.0	0.9	11.4	2.2	16.2	2.4	—	—	-0.7	0.2
mips003832	53.1983	-27.7478	272.0	33.3	13.4	1.3	15.2	1.5	16.0	2.5	21.0	2.7	—	—	-0.5	0.2
mips003871	53.1379	-27.7002	183.0	35.1	12.4	1.2	10.4	1.1	15.0	2.5	17.9	2.5	7145.0	2201.8	-0.5	0.2
mips004100	52.9933	-27.7934	95.9	24.5	4.7	0.5	4.3	0.5	5.9	1.9	10.7	2.1	—	—	-0.9	0.3
mips004104	52.9897	-27.7513	146.0	31.2	13.0	1.2	13.6	1.4	23.6	3.1	21.2	2.7	—	—	-0.8	0.2
mips004127	52.9616	-27.7844	369.0	40.8	17.0	1.6	17.5	1.7	17.2	2.6	30.4	3.4	3006.1	2282.5	-0.7	0.2
mips004145	53.2298	-27.7087	177.0	43.9	5.6	0.6	7.8	0.8	10.5	2.2	22.0	2.8	—	—	-1.7	0.2
mips004158	53.2556	-27.6788	596.0	70.7	63.7	5.9	63.2	6.2	77.7	8.5	121.0	11.2	6698.8	2231.5	-0.8	0.2
mips004196	53.0794	-27.7416	253.0	28.5	6.8	0.7	10.7	1.1	22.7	3.1	35.9	3.8	—	—	-2.1	0.2
mips004244	52.9554	-27.7692	195.0	31.3	13.8	1.3	13.3	1.4	24.0	3.2	21.0	2.7	—	—	-0.7	0.2
mips004982	52.9825	-27.6782	279.0	33.0	10.2	1.0	11.8	1.2	19.5	2.8	19.6	2.6	6652.7	2234.0	-0.9	0.2
mips005020	53.0775	-27.6349	289.0	37.2	5.4	0.6	7.1	0.8	11.4	2.2	22.7	2.8	4775.3	2040.7	-1.8	0.2
mips005025	52.9845	-27.6672	215.0	28.7	17.1	1.6	19.5	1.9	27.9	3.5	25.0	3.0	—	—	-0.6	0.2
mips005381	53.0331	-27.6256	946.0	60.1	49.4	4.6	54.3	5.3	89.7	9.7	173.0	16.1	—	—	-1.6	0.2
mips009632	53.2606	-27.9459	255.0	31.8	11.4	1.1	11.7	1.2	13.1	2.3	19.1	2.6	—	—	-0.6	0.2
mips009713	52.9383	-27.8845	180.0	31.0	8.1	0.8	9.2	1.0	11.2	2.2	15.1	2.4	—	—	-0.8	0.2
mips009742	53.2202	-27.7456	119.0	28.7	6.5	0.7	6.4	0.7	10.6	2.2	10.4	2.1	—	—	-0.7	0.3
mips009751	53.2235	-27.7151	209.0	30.2	8.0	0.8	8.3	0.9	15.1	2.5	13.7	2.3	—	—	-0.8	0.2
mips009834	53.1158	-27.6306	1120.0	73.6	157.0	14.5	175.0	17.0	209.0	22.2	306.0	28.2	6823.4	2012.8	-0.8	0.2
mips010694	53.1030	-27.8930	241.0	37.5	9.0	0.9	10.2	1.1	12.6	2.3	19.1	2.6	—	—	-0.9	0.2
mips010818	53.1134	-27.6811	171.0	32.8	8.9	0.9	10.3	1.1	17.1	2.6	17.1	2.5	5675.4	2204.1	-0.9	0.2
mips013065	53.1754	-27.6949	146.0	26.7	9.2	0.9	12.8	1.3	15.0	2.5	21.9	2.8	8072.4	2320.3	-1.1	0.2
mips013589	52.9784	-27.8949	273.0	41.3	14.3	1.4	15.6	1.6	24.1	3.2	20.9	2.7	—	—	-0.6	0.2

Notes.— Column (1): MIPS 24 μm name. Columns (2) and (3): MIPS 24 μm J2000.0 RA and Dec. Columns (4) and (5): MIPS 24 μm flux density and error. Columns (6) through (13): IRAC flux densities and errors. Columns (14) and (15): MIPS 70 μm flux density and error. Columns (16) and (17): IRAC spectral index and uncertainty.

Table 2: X-ray properties of the IR power-law galaxy sample.

Name	$f_{0.5-8\text{keV}}$ erg cm ⁻² s ⁻¹	$f_{0.5-2\text{keV}}$ erg cm ⁻² s ⁻¹	$f_{2-8\text{keV}}$ erg cm ⁻² s ⁻¹	Γ	off-axis angle	ID
(1)	(2)	(3)	(4)	(5)	(6)	(7)
mips000243	0.2650E-14	0.7800E-15	0.1900E-14	1.39	7.95	A277
mips000309	0.1210E-12	0.4940E-13	0.6860E-13	1.79	7.53	A177
mips000348	0.1090E-13	0.1530E-14	0.9400E-14	0.73	10.09	A310
mips002310	0.2400E-14	0.3080E-15	0.2050E-14	0.67	8.04	A92
mips002707	0.1390E-13	0.3970E-14	0.9480E-14	1.40	9.16	A322
mips002775	0.9670E-14	0.3890E-15	0.9890E-14	-0.31	6.89	A302
mips002886	0.6430E-15	-0.1390E-15	-0.9690E-15	1.40	8.19	S1
mips003108	0.5730E-14	0.1670E-14	0.3820E-14	1.43	4.57	A251
mips003133	0.2270E-15	-0.7880E-16	-0.4530E-15	1.40	4.93	S2
mips003149	0.1750E-15	-0.6840E-16	-0.4550E-15	1.40	5.29	S3
mips003175	0.3320E-14	0.5430E-15	0.2760E-14	0.86	5.82	A59
mips003412	0.1000E-13	0.1610E-14	0.8640E-14	0.82	8.07	A16
mips003445	0.9000E-15	0.1610E-15	-0.8960E-15	1.40	7.83	A22
mips003467	0.1580E-14	-0.1340E-15	0.1100E-14	0.00	9.10	G319
mips003485	-0.1970E-15	0.5320E-16	-0.3220E-15	1.40	3.96	A165
mips003528	-0.1730E-15	0.4600E-16	-0.3850E-15	1.40	2.01	S4
mips003554	0.3640E-14	0.1280E-14	0.2170E-14	1.65	7.26	A45
mips003559	0.4010E-14	0.6380E-15	0.3470E-14	0.82	8.07	A36
mips003618	0.7760E-15	0.5430E-16	0.7010E-15	0.19	1.78	A219
mips003636	0.1690E-14	0.2830E-15	-0.1330E-14	0.92	9.36	A14
mips003674	0.1000E-13	0.2240E-14	0.7480E-14	1.17	6.94	A30
mips003735	0.7910E-14	0.3180E-14	0.4750E-14	1.74	10.63	A323
mips003777	0.1720E-14	0.4210E-15	-0.1420E-14	1.16	10.06	A3
mips003888	0.1160E-13	0.4880E-15	0.1160E-13	-0.25	6.86	A179
mips003915	0.3220E-13	0.1600E-13	0.1550E-13	2.05	9.12	A234
mips003938	0.2480E-15	0.6340E-16	-0.3270E-15	1.40	2.34	A197
mips004254	0.3950E-14	0.1170E-14	0.2730E-14	1.42	8.81	A7
mips004258	0.1640E-13	0.6140E-14	0.9810E-14	1.69	5.80	A76
mips004281	0.1450E-14	0.2340E-15	0.1190E-14	0.86	7.46	A60
mips005415	0.2920E-14	-0.1570E-14	-0.6340E-14	1.40	12.39	S7
mips009708	0.1010E-13	0.3660E-14	0.6110E-14	1.66	3.38	A256
mips009714	0.1450E-13	0.4000E-14	0.1020E-13	1.36	10.15	A4
mips009757	0.7030E-14	0.1900E-15	0.7260E-14	-0.61	4.52	A268
mips010697	0.1520E-13	0.5970E-14	0.8780E-14	1.75	4.17	A230
mips010760	-0.1450E-15	0.3060E-16	-0.2020E-15	1.40	3.22	S8
mips010785	0.6120E-14	0.1090E-14	0.4940E-14	0.94	5.54	A166
mips010787	0.6320E-14	0.2790E-14	0.3350E-14	1.90	6.33	A163
mips010823	0.1010E-13	0.2630E-14	0.7030E-14	1.32	8.39	A174
mips012254	0.1930E-13	0.7420E-14	0.1150E-13	1.71	7.04	A305
mips012297	0.3790E-13	0.7920E-14	0.2960E-13	1.08	7.46	A274
mips012310	0.3370E-14	0.1200E-15	0.3620E-14	-0.43	5.39	A50
mips012314	0.2170E-14	0.4930E-15	0.1570E-14	1.20	7.97	A15
mips012329	0.7060E-14	-0.3650E-15	0.8340E-14	-0.23	9.06	A278
mips012371	0.3110E-13	0.1260E-13	0.1800E-13	1.77	9.48	A109
mips012940	0.4610E-13	0.1190E-13	0.3110E-13	1.34	12.17	A313
mips013087	0.2490E-13	0.1280E-13	0.1180E-13	2.08	8.02	A173
mips013611	0.1150E-12	0.4460E-13	0.6770E-13	1.73	4.45	A66
mips014534	0.6980E-14	0.1620E-14	0.5630E-14	1.13	9.14	A38
mips014635	0.2130E-13	0.7770E-14	0.1290E-13	1.66	3.14	A191

Table 2: Continued.

Name	$f_{0.5-8\text{keV}}$ erg cm ⁻² s ⁻¹	$f_{0.5-2\text{keV}}$ erg cm ⁻² s ⁻¹	$f_{2-8\text{keV}}$ erg cm ⁻² s ⁻¹	Γ	off-axis angle	ID
(1)	(2)	(3)	(4)	(5)	(6)	(7)
mips000314	-0.4490E-15	-0.1330E-15	-0.7780E-15	1.40	8.33	-
mips002219	-0.6670E-15	-0.1970E-15	-0.1150E-14	1.40	10.27	-
mips002556	-0.9110E-15	-0.2290E-15	-0.1750E-14	1.40	10.43	-
mips002581	-0.8460E-15	-0.2110E-15	-0.1530E-14	1.40	10.72	-
mips002613	-0.6160E-15	-0.1710E-15	-0.1090E-14	1.40	9.41	-
mips002788	-0.6640E-15	-0.2010E-15	-0.1150E-14	1.40	9.98	-
mips002957	-0.4670E-15	-0.1440E-15	-0.8110E-15	1.40	8.36	-
mips003068	-0.2590E-15	-0.5460E-16	-0.5220E-15	1.40	6.47	-
mips003181	-0.1900E-15	-0.5910E-16	-0.3140E-15	1.40	3.96	-
mips003182	-0.2330E-15	-0.7700E-16	-0.3620E-15	1.40	5.23	-
mips003271	-0.7730E-14	-0.9990E+03	-0.1130E-13	1.40	11.96	-
mips003357	-0.5570E-15	-0.1350E-15	-0.1040E-14	1.40	9.38	-
mips003363	-0.5170E-15	-0.1400E-15	-0.9240E-15	1.40	9.11	-
mips003377	-0.4600E-15	-0.1340E-15	-0.8290E-15	1.40	8.32	-
mips003395	-0.3640E-15	-0.9990E-16	-0.6620E-15	1.40	7.70	-
mips003454	-0.4800E-15	-0.1170E-15	-0.9310E-15	1.40	9.25	-
mips003480	-0.4920E-15	-0.1290E-15	-0.9350E-15	1.40	8.45	-
mips003537	-0.1290E-15	-0.7300E-16	-0.2660E-15	1.40	2.89	-
mips003556	-0.3160E-15	-0.8700E-16	-0.5710E-15	1.40	7.18	-
mips003639	-0.3170E-15	-0.9600E-16	-0.5440E-15	1.40	7.05	-
mips003641	-0.3060E-15	-0.8010E-16	-0.5430E-15	1.40	7.00	-
mips003832	-0.2160E-15	-0.6230E-16	-0.3990E-15	1.40	5.69	-
mips003871	-0.3310E-15	-0.9010E-16	-0.5870E-15	1.40	6.69	-
mips004100	-0.2690E-15	-0.7040E-16	-0.5090E-15	1.40	6.67	-
mips004104	-0.3580E-15	-0.9600E-16	-0.6200E-15	1.40	7.65	-
mips004127	-0.4720E-15	-0.1240E-15	-0.8560E-15	1.40	8.42	-
mips004145	-0.7470E-15	-0.2060E-15	-0.1320E-14	1.40	8.52	-
mips004158	-0.1510E-13	-0.4140E-14	-0.2670E-13	1.40	10.76	-
mips004196	-0.2010E-15	-0.6200E-16	-0.3750E-15	1.40	4.58	-
mips004244	-0.5780E-15	-0.1750E-15	-0.1010E-14	1.40	8.95	-
mips004982	-0.1480E-14	-0.4780E-15	-0.2520E-14	1.40	10.68	-
mips005020	-0.1830E-14	-0.4990E-15	-0.3090E-14	1.40	10.73	-
mips005025	-0.1950E-14	-0.4810E-15	-0.3620E-14	1.40	11.11	-
mips005381	-0.1430E-13	-0.3330E-14	-0.2560E-13	1.40	11.95	-
mips009632	-0.2820E-14	-0.7950E-15	-0.4600E-14	1.40	11.14	-
mips009713	-0.8010E-15	-0.2180E-15	-0.1480E-14	1.40	10.51	-
mips009742	-0.3260E-15	-0.7670E-16	-0.6190E-15	1.40	6.69	-
mips009751	-0.4550E-15	-0.1140E-15	-0.8730E-15	1.40	8.01	-
mips009834	-0.3930E-14	-0.1530E-14	-0.6610E-14	1.40	10.78	-
mips010694	-0.2060E-15	-0.5030E-16	-0.3930E-15	1.40	5.03	-
mips010818	-0.4000E-15	-0.1380E-15	-0.6350E-15	1.40	7.75	-
mips013065	-0.3700E-15	-0.9570E-16	-0.6880E-15	1.40	7.56	-
mips013589	-0.4810E-15	-0.1330E-15	-0.8790E-15	1.40	8.96	-

Notes. — Column (1): MIPS 24 μm name. Column (2): *Chandra* full-band 0.5 – 8 keV flux or upper limit. Column (3): *Chandra* soft-band 0.5 – 2 keV flux or upper limit. Column (4): *Chandra* hard-band 2 – 8 keV flux or upper limit. Negative values for the fluxes mean upper limits. Column (5): Photon index, for the sources not detected in all three *Chandra* bands, the photon index is assumed to be $\Gamma = 1.4$. Column (6): Off-axis angle in arcmin. Column (7): If an ID is given, cross-identification with a previously published X-ray source. Source IDs starting with an 'A' are from the Alexander et al. (2003a) catalog, source ID G319 is from the Giacconi et al. (2002) catalog, and source IDs starting with 'SUPP' are from the supplementary (unpublished data) catalog (see text for details).